Master Thesis

Development of an Elasto-Damage Constitutive Law for Implicit Finite Element Methods

carried out for the purpose of obtaining the degree of Master of Science (Dipl.-Ing.),
submitted at TU Wien, Faculty of Mechanical and Industrial Engineering, by

Andreas Wagner

Mat.Nr.: 01327503

under the supervision of
Associate Prof. Dipl.-Ing. Dr.techn. Heinz Pettermann
Institute of Lightweight Design and Structural Biomechanics, E317

Vienna, September 2020

Affidavit

I declare in lieu of oath, that I wrote this thesis and performed the associated research by myself, using only literature cited in this volume.

Signature:

Date:

Acknowledgments

This work was carried out at the Institute of Lightweight Design and Structural Biomechanics (ILSB) at the Vienna University of Technology.

I want to express my gratitude to all ILSB members for creating a supportive working environment and for giving me the opportunity to write my master thesis. Special thanks to my thesis advisors Professor Heinz Pettermann and Univ.Ass. Jan Kaul, who contributed with their vital guidance to the successful conclusion of this work.

Last but not least, I want to thank my family and friends who supported me during the entirety of my academic education, without them I would not be where I am today.

Abstract

Cracks and similar defects have a strong influence on the structural behavior, thus it is of great interest to analyze the development of material damage. Typically methods such as linear elastic fracture mechanics and the J-integral are used to describe fracture processes. However, these approaches are hardly applicable for problems with complex geometry and crack patterns. This is where continuum damage mechanics shows its strength, as it allows the treatment of complicated problems in a non-linear numerical context. In this spirit, a continuum damage mechanics based elasto-damage constitutive law for implicit finite element methods is developed, implemented, and tested within the scope of this thesis. Implementation in Abaqus/Standard 2018 by Dassault Systèmes is done via the user material subroutine. The model is intended for the simulation of damage development in brittle and quasi-brittle materials such as concrete.

The implemented isotropic damage model features a single scalar damage variable and a linear strain-softening behavior. General strain states are treated by calculating a scalar measure from the strain tensor called equivalent strain, which is obtained by using the energy norm. Viscous regularization, which adds an artificial viscous behavior, ensures that converging results are obtained. Mesh-size sensitivity typically encountered in finite element simulations of strain-softening materials is addressed with mesh-adjusted softening regularization. This method incorporates the specific fracture energy and the characteristic element length into the constitutive behavior, where the post-peak softening slope is adjusted in such a manner that mesh-size independent energy dissipation and objective load-displacement results are obtained.

The numerical results are in good agreement to literature references given for concrete structures. Despite the basic similarities, however, the results also exhibit certain differences compared to the literature references attributed to a differently modeled softening regime. While the strain-softening behavior is linear in the implemented model, it is exponential in the literature references. Nevertheless, the developed damage model represents a general elasto-damage constitutive law, thus the chosen linear strain-softening type is justified. In conclusion, the developed damage model is suitable to simulate damage development in brittle and quasi-brittle materials. Nevertheless, it is important that the requirements imposed by the mesh-adjusted softening regularization are fulfilled, and to bear in mind that the linear strain-softening is just a simple approximation of the post-peak behavior.

Kurzfassung

Risse und ähnliche Defekte haben einen starken Einfluss auf das strukturelle Verhalten, somit ist es von großem Interesse die Entstehung von Materialschädigung zu untersuchen. Klassischerweise werden Methoden wie die linear-elastische Bruchmechanik und das J-Integral-Verfahren verwendet um Bruchprozesse zu beschreiben. Allerdings sind diese Ansätze kaum anwendbar für Problemstellungen mit komplexer Geometrie und verzweigtem Risswachstum. Hier zeigt die Kontinuums-Schädigungsmechanik ihre Stärken, indem sie die Behandlung von komplizierten Problemstellungen im Rahmen einer nicht-linearen numerischen Simulation ermöglicht. In diesem Sinne wird im Rahmen dieser Diplomarbeit ein Elasto-Schädigungs-Konstitutivgesetz basierend auf Kontinuums-Schädigungsmechanik für implizite Finite Elemente Methoden entwickelt, implementiert und getestet. Die Implementierung in Abaqus/Standard 2018 von Dassault Systèmes wird mittels der User Material Subroutine durchgeführt. Der beabsichtige Verwendungseinsatz dieses Schädigungsmodells ist die Simulation von Materialschädigung in spröden und quasi-spröden Werkstoffen wie Beton.

Das implementierte isotrope Schädigungsmodell verwendet eine einzelne skalare Schädigungsvariable und eine lineare mechanische Entfestigung. Allgemeine Verzerrungszustände werden behandelt indem eine skalare Vergleichsgröße, die sogenannte äquivalente Dehnung, von dem Verzerrungstensor durch Verwendung der Energie-Norm berechnet wird. Viskose Regularisierung fügt dem Modell eine künstliche Viskosität hinzu, welche benötigt wird um konvergierende Lösungen zu erhalten. Die ausgeprägte Sensibilität der Lösung bezüglich der Netzgröße, welche typisch ist für die Finite Elemente Simulation von Entfestigunsproblemen, wird durch netzangepasste mechanische Entfestigung behandelt. Diese Methode berücksichtigt die spezifische Bruchenergie und die charakteristische Elementgröße

in den Konstitutivgleichungen und skaliert die Entfestigung derart, dass die numerische Lösung unabhängig ist von der Netzgröße.

Die numerischen Resultate sind in guter Übereinstimmung zu Literatur Referenzbeispielen für Strukturen aus Beton. Dennoch sind gewisse Unterschiede zu den Literaturbeispielen vorhanden, welche einem unterschiedlich implementierten Entfestigungsverhalten geschultet sind. Während das implementierte Entfestigungsverhalten linear ist, wurde in den Referenzbeispielen ein exponentieller Ansatz verwendet. Nichtsdestotrotz ist die Implementierung des linearen Ansatzes gerechtfertigt, da ein allgemeines Elasto-Schädigungs Konstitutivgesetz entwickelt wurde. Abschließend kann gesagt werden, dass das entwickelte Schädigungsmodell geeignet ist um die Entstehung und Entwicklung von Materialschäden in spröden und quasispröden Werkstoffen zu simulieren. Jedoch muss darauf geachtet werden, dass die Anforderungen welche durch die verwendete netzangepasste mechanische Entfestigung entstehen auch eingehalten werden. Des Weiteren stellt die verwendete lineare Entfestigung nur eine grobe Näherung des Schädigungsverhaltens dar.

Contents

List of Figures

1. Introduction

In this chapter, a short overview of the historical developments in the analysis of fracture processes and the modeling of damage formation is given. Furthermore, the influence of dramatic material failures in the 20th century on the development of a new scientific field called fracture mechanics is highlighted. The insights gained from this new school of thought led to more accurate strength predictions for structural components, however, the necessary assumptions for its application are not fulfilled by many materials. This problem combined with the rapid advances in computing performance led to the development of several numerical approaches for simulating damage and fracture. Additionally, the motivation behind these numerical modeling techniques is highlighted and the main task of this thesis described. The methodological approach and the structure of this thesis is given at the chapters end.

1.1. Aim of the thesis

The aim of this thesis is to develop an elasto-damage constitutive-law for implicit FEM, which is to be implemented in the commercial software Abaqus/Standard via the user-material subroutine UMAT. The model is intended for materials that behave linear elastic up to the ultimate strength, beyond which quasi-brittle failure with negligible amounts of plastic deformation takes place. Typical examples for materials with such a strain-softening behavior are concrete, ceramics, and rocks. A continuum damage mechanics based modeling approach is chosen since it is simple to implement within a standard finite element environment. However, a number of problems such as numerical instability and mesh-sensitivity have to be addressed in order to obtain meaningful results [23]. Since the material is described by means of continuum mechanics, damage formation must be considered smeared, which works well in cases of distributed micro-cracking but is not limited to distributed cracking.

For the sake of simplicity, isotropic material behavior is assumed both in the initial and in the damaged state. Thus the directional nature of microcrack-like defects is entirely neglected. A single scalar damage variable is used to model isotropic damage as stiffness degradation. The resulting material damage model is obtained by scaling the initial linear-elastic isotropic constitutive-law with a scalar-valued function that describes the extent of damage. The onset and development of damage are assumed to be exclusively strain-driven, where the initiation criterion and the evolution function are derived from a predefined stress-strain diagram. The mechanical response of the material is defined by this diagram, which exhibits linear elastic and linear strain-softening behavior. For general stress states, the damage variable is evaluated with a scalar measure for the strain state, called equivalent strain $\varepsilon_{\mathrm{equ}}$. Finally the question of suitability is addressed, to assess whether or not this simple isotropic model can produce reliable predictions for simulating damage and fracture formation in quasi-brittle materials, such as concrete.

1.2. Importance of Damage Modeling

Simulation of damage processes leads to a better understanding of the mechanical behavior beyond the linear elastic behavior, and may give an estimate for the most likely way a component or structure will fail. Additionally the load-displacement behavior and therefore the total amount of dissipated energy during fracture can be obtained with numerical simulations. An accurate prediction of crack growth helps to determine the damage tolerance, which is an especially important characteristic of brittle structures. In some cases the problem can be analyzed sufficiently with the classical linear elastic fracture mechanics method (LEFM), but quite often the required conditions for its application are not fulfilled. Meaningful results in LEFM are only obtained when the material behaves linearly except in a zone of very small size at the crack tip [6]. Another downside of LEFM is that it requires a predefined crack path, which must be known a priori or determined using additional theories. Whenever the volume region affected by dissipative mechanisms such as the formation of microcracks is too large for the application of LEFM, different methods must be used. Alternative approaches for these cases include nonlinear fracture mechanics, J-Integral, and numerical damage modeling. Especially the latter approach is promising since these analytical methods are quite cumbersome. Nevertheless, the use of numerical approaches such as continuum damage mechanics is not restricted to cases where LEFM cannot be used. Numerical damage models applied in a nonlinear simulation allow the analysis of complex fracture problems, either with or without plastic deformation, featuring ductile, brittle or quasi-brittle damage development.

1.3. Historical Overview on the Analysis of Fracture Processes and Damage Modeling

Analysis of fracture processes leads to a better understanding of the behavior and influence of material defects. Thus it helps to predict whether or not these flaws grow under certain circumstances. The knowledge of the material flaw behavior helps to define a relation between the applied loads and the defect size, which allows the definition of the maximum allowable load for a given defect and vice versa [6]. Since defects are always introduced during the manufacturing process, the analysis of them is therefore of great interest in mechanical engineering. Fracture analysis plays an especially important role in brittle materials, that lack mechanisms to dissipate large amounts of energy, which results in a poor crack growth resistance. These materials can therefore fail quite suddenly without any warning signs, which led to many spectacular and dramatic cases of material failure in the 20th century [6]. A very prominent example is the brittle fracture of the Liberty Cargo Ships built during World War II, that failed under stress conditions well below the critical limit defined by classical material strength analyses, such as the maximum principal stress criterion [6]. These historic events helped that the scientific community acknowledged material defects as the original cause of failure and contributed to the rise of damage tolerance analyses and the fracture mechanics method [6].

The fracture mechanics method can be traced back to Griffith [2], who published a paper on the brittle fracture of glass in 1920. His work is inspired by the fact that the theoretical strength of glass, defined by the atomic bonds, is approximately two orders of magnitude larger than the experimentally obtained value. He concluded that material defects are responsible for this huge discrepancy as they cause stress concentrations. His experiments showed a strong correlation between defect size and fracture stress that depends on the surface energy γ needed for a crack extension [6]. Griffith's theory yields accurate results for brittle materials such as glass, but not in cases of ductile failure nor for quasi-brittle materials that only appear to be brittle. Therefore, his work has not found much attention until Irwin [13] adapted it in the 1950s. He introduced the stress intensity factor K_I and the strain energy release rate G_I, which are the two available concepts of classical fracture mechanics up to this day. While ($G_\mathrm{I} = -\frac{dU}{da}$) describes the elastic energy released upon crack growth, K_I is a measure of the stress intensity at the crack tip [6]. Both parameters can be determined analytically and converted from one to the other. Irwin defined two failure criteria that predict crack growth if these parameters become equal to newly defined fracture toughness material constants ($K_\mathrm{I} = K_\mathrm{Ic}$) and ($G = G_\mathrm{Ic}$) [6]. Both approaches yield reliable results in many fracture problems of predominantly brittle materials. Nevertheless, Irwin's linear elastic fracture mechanics approach (LEFM) still relies on the small-scale yielding assumption, according to which the zone of plastic deformation at the crack tip is small compared to the size of the crack itself [6]. Since this is not the case for materials that exhibit the formation of a so-called fracture process zone (FPZ) or display pronounced plasticity, LEFM cannot be applied in many problems. This resulted in the development of different approaches such as numerical fracture and damage simulations.

Numerical damage models have been developed since the early 1960s, including different approaches in the context of material and crack representation, such as continuum mechanics based and discrete descriptions both for the bulk material and the crack itself. One of the first approaches is the cohesive-zone model (CZM), independently developed by Dugdale [9] (1960) and Barenblatt [12] (1962) for elastic-plastic failure, which was adapted for quasi-brittle materials by Hillerborg et al. [1] in 1976, who introduced the fictitious crack model. He included fracture mechanics in the numerical modeling approach in terms of the specific fracture energy [24]. The cohesive zone and fictitious crack model are extensions to the LEFM method and describe fracture as a gradual phenomenon, where cohesive surfaces are separated. The material is assumed to loose its ability to transfer stress across a developing crack in dependence of the crack opening width, described by a traction-separation law. An important advantage of these cohesive approaches compared to LEFM is that they include an intrinsic fracture energy dissipation mechanism [6]. A material that is regularly in the focus of research is concrete, as it is one of the most commonly used construction materials. The complexity of its heterogeneous microstructure, consisting of mortar and aggregates, necessitates a numerical treatment [23]. Two of the earliest models developed for simulating damage and fracture specifically for concrete, are the discrete crack and the smeared crack approach introduced in the 1960s. The numerical results of early smeared crack approach simulations have shown a mesh-sensitivity, which has been addressed by Bazant and Oh [37] who introduced the crack band model [28] [10].

Another numerical modeling technique is continuum damage mechanics (CDM). It is similar to the smeared crack approach, which can be regarded as a special case of an anisotropic CDM model [32] [25] [37]. The effects of microstructural damage are described on the continuum level with a finite number of scalar or tensor-valued internal variables [28]. The method was introduced by Kachanov [19] in 1958 and modified by Rabotnov [35] ten years later, who introduced a scalar measure called damage variable that describes the effects of damage on the mechanical behavior [17] [23]. Due to its simplicity and good compatibility with the standard finite element method [21], CDM became very popular and was further improved up to this day.

A more recent development in fracture analysis is the extended finite element method (XFEM) introduced in 1999 by Belytschko et al. [33], which uses discontinuity embedded interpolation functions. This method models fracture as displacement jump contained inside of the element with arbitrary orientation. It can be used in conjunction with LEFM or cohesive zone modeling approaches.

1.4. Methodological Approach

In order to fulfill the objective of this thesis, namely developing a numerical material model for predicting elasto-damage failure by means of implicit FEM, a literature study is conducted at first. Based on this, the modeling approach is chosen, implemented, applied to problems, and its results compared with literature references. To give a better overview, the content and structure of this thesis is outlined in the following.

The relevant theoretical aspects of damage and fracture are reviewed in Chapter 2, where different types of numerical damage models are compared as well. Based on the reviewed literature, a continuum damage mechanics based modeling approach is chosen, which allows a simple implementation in the context of standard finite element analyses. The foundations of continuum damage mechanics, typical issues encountered, and some approaches to address them are described in chapter 3. Abaqus/Standard, a commercial implicit FEM software package by Dassault Systemes, is used as simulation environment. It allows the application of any user-defined constitutive law via the UMAT user-subroutine. Implementation of the chosen modeling approach is given in chapter 4. For the sake of brevity, the developed model is limited to standard 3D continuum, 2D plane-strain, and beam elements. Simple simulation models, such as a uniaxial tensile test and three-point bending tests are used to test the developed elasto-damage constitutive law. The numerical results obtained with the developed material model are compared to published literature references in chapter 5. Finally a summary and conclusion is given in chapter 6, where additional remarks regarding possible improvements, alternative approaches, and further research are listed as well.

2. Aspects of Damage, Fracture and their Modeling

As explained in the previous Chapter, the processes of fracture and damage formation have been in the focus of engineering science ever since dramatic material failures in the twentieth-century. A new field of research named fracture mechanics arose, which aims at explaining the growth of macroscopic cracks. Comparing experimentally obtained fracture resistance parameters to analytically derived fracture driving forces, this research field helps to gain vital insights. Different approaches for the analysis of fracture processes are available, such as the classical linear elastic fracture mechanics (LEFM), J-integral, numerical methods like cohesive zone models, and many others. While LEFM is limited to cases with small-scale yielding [6], the J-integral approach can be used in cases exhibiting more ductile failure. Nevertheless, these analytical methods are quite cumbersome and therefore limited to cases with rather simple geometry and crack paths. Numerical methods on the other hand represent a promising tool for the analysis of problems with more complex geometry and crack paths.

The separation of a solid into two or more pieces is called fracture, thus is it can be regarded as the final stage in the damage process. Damage on the other hand, is a synonym for all the defects causing loss of material integrity, resulting in a reduction of load-bearing ability and stiffness. These stress-driven defects are typically caused by mechanisms such as the nucleation, propagation, and coalescence of microcracks and microvoids [3]. The extent of damage formation is influenced by the loading-conditions, temperature, and of course the material itself. In this context, a fitting definition for damage has been given by Lemaitre [18], who states, *“damage of materials is the progressive physical process by which they break”*.

2.1. Fracture Modes and Failure Types

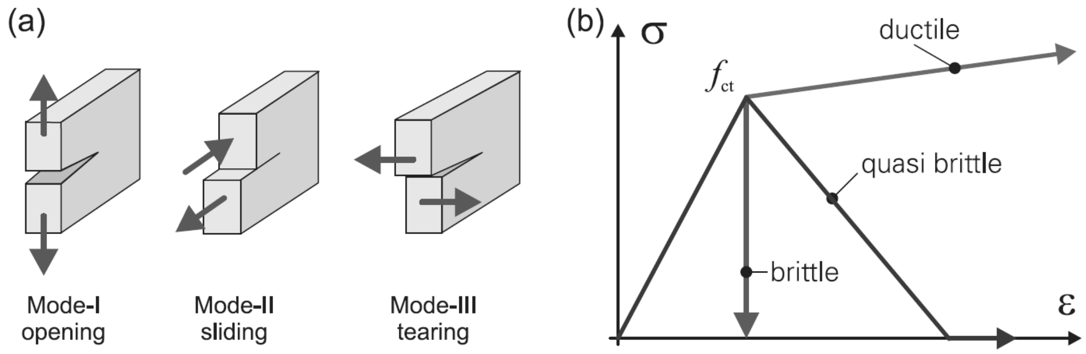

Figure 2.1.: (a) Fracture Modes. (b) Material failure types (figure is modified in contrast to literature reference) [34].

The formation of a macroscopic crack leads to the separation of fractured surfaces. Three fracture modes can be distinguished depending on the relative separation direction, shown in Figure 2.1 (a). Any fracture in a solid may be described by one of these modes, or their combinations [6].

- **Mode-I (Opening Mode):** the separation of cracked surfaces happens normal to the crack-plane [6].
- **Mode-II (Sliding Mode):** the displacement jump is in-pane with the crack-plane and perpendicular to the crack front [6].
- **Mode-III (Tearing Mode):** a parallel to the crack front and in-plane separation leads to tearing [6].

Depending on the degree of plastic deformation and the amount of dissipation prior to final rupture, the fracture behavior shown in figure 2.1 (b) can be categorized as ductile, brittle, or quasi-brittle. As can be seen, ductile failure is accompanied by large amounts of plastic deformation and dissipated energy, represented by the area under the stress-strain curve minus the elastic strain energy density. This type of failure is typical for many metals [23]. The energy is dissipated by the movement and creation of dislocations, which is accompanied with a hardening effect. Therefore materials with this failure type exhibit stress-strain curves with a positive slope beyond the yield limit. Typical defects are the formation and growth of spherical and ellipsoidal microvoids [23], which can be seen as dimples on the fracture surfaces.

Brittle failure on the other hand, is characterized by macroscopically undeformed fracture surfaces [23]. Furthermore, the amount of dissipated energy is explicitly defined by the surface energy γ needed for crack extension [17] [23], which is rather small. Therefore this type of failure shows a sudden drop in the stress-strain diagram, a behavior which is typically encountered in glass [23]. In contrast to this extreme case, many materials only appear to be brittle in terms of macroscopic deformation, but can dissipate significant amounts of energy during the fracture process [23]. This type of failure is called quasi-brittle and is produced by the formation of numerous microcracks in a region close to the crack-tip called fracture process zone [17]. Materials with quasi-brittle failure show a gradual decrease in stress when the strain is increased beyond the ultimate strength, which is called strain-softening behavior. Typical examples are concrete, ceramics and rocks [17] [23] [21]. It should be noted though, that the type of failure is also influenced by other factors such as temperature, loading-rate, and stress triaxiality the same material can response either ductile or brittle depending on the circumstances [17].

2.2. Effects of Damage

Material damage affects the mechanical behavior already in the early stage of microcrack and microvoid formation, which reduces the effectively load-bearing cross-section. The most common effects of damage are stiffness deterioration [27] [37], reduction of material strength, and damage-induced anisotropy, which are further explained in the following.

2.2.1. Stiffness Deterioration

In comparison to the undamaged state, less atomic bonds are available to transfer the applied loads in the damaged situation. This results in larger strain

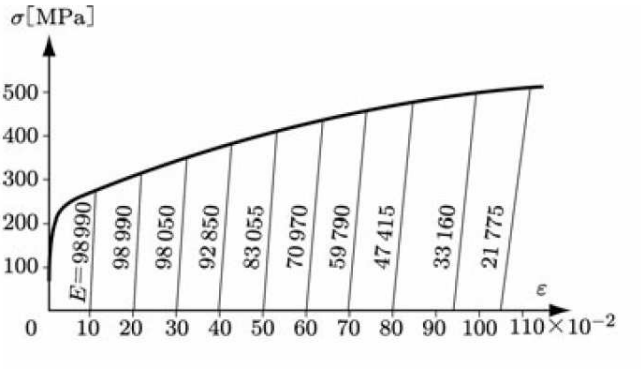

Figure 2.2.: Stress-strain diagram showing the stiffness degradation due to damage formation in copper [23].

values for the same externally applied load, because the relative separation of the remaining atomic bonds increases in order to withstand the larger force per bond. This indicates that the macroscopically observed stiffness is reduced by damage formation [27] [37]. When the specimen in a uniaxial tensile test is unloaded after damage has been formed, the reduced stiffness can be observed in a less steep slope in the stress-strain diagram, as can be seen in figure 2.2 (a). Furthermore, the diagram shows that damage forms only beyond a certain level of plastic deformation in materials with ductile failure, which can be seen in (b) as well. The reason for this behavior is the circumstance that plastic deformation does not lead to the breakage of atomic bonds below a certain value [17]. This is not the case, when brittle and quasi-brittle failure is treated, where the inelastic strains are caused by microcrack formation, which is inevitably accompanied by stiffness reduction [17] [23].

2.2.2. Reduction of Material Strength

In addition to the stiffness deterioration, the reduction of effective area also magnifies the stress acting on the not yet damaged regions, which is then called effective stress σ_{eff} [14]. For quasi-brittle materials that lack hardening mechanisms, this inevitably leads to a reduction of macroscopically observed material strength [14]. This behavior, shown in figure 2.3, is called strain-softening and can be

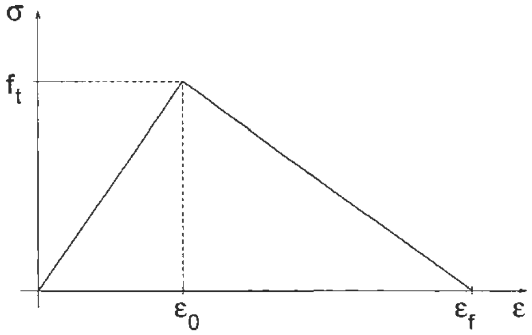

Figure 2.3.: Stress-strain diagram of a brittle material exhibiting linear strain-softening behavior [20].

regarded as material instability [23]. It may even lead to a unstable structural response [14].

2.2.3. Damage-induced Anisotropy

Depending on the material and stress state, different types of defects with a certain orientation and distribution may form. While homogeneously dispersed spherical voids preserve an initial isotropic material behavior, any deviation from such an idealized state will lead to damage-induced anisotropy. The complexity and difficulties involved in the numerical implementation of the directional behavior are the most challenging tasks when defining a material damage model. Brittle and quasi-brittle materials predominantly exhibit crack-like defects, which results in a pronounced anisotropic behavior [23]. A typical directional behavior introduced by microcracks is the so-called unilateral effect, which describes the different mechanical behavior depending on the loading-direction [23] [17]. While cracks reduce the effective area under tensile load, they may close again when the load is reversed. Therefore, some of the stiffness and strength reduction observed under tensile stress are regained again when the crack closes under compressive load. This effect is also known as crack-closure or stiffness-recovery. Although cracks develop with an apparent orientation, the damage process may still be assumed to be isotropic in cases of proportional loading without falsifying the results too much [23].

2.2.4. Size-Effect

Materials with predominantly brittle and quasi-brittle failure are very defect-sensitive, which results in a dependence of the observed material strength on the component size [5]. This so-called size-effect results from the increased probability that a large defect with harmful orientation and location is present. While ductile materials can counter the stress-magnifying effects of such defects with plastic deformation and energy dissipation, brittle and quasi-brittle are much more prone to them. Another difficulty resulting from the size-effect is that it poses a source of uncertainty, since the material parameters obtained from a small test specimen have to be extrapolated [17].

2.2.5. Scale of damage phenomena and mechanisms

The phenomena linked with damage formation result from mechanisms acting on very different size scales, which are shown in figure 2.4. The damage process begins with the splitting of atomic bonds and leads in its final stage to the formation of macroscopic cracks with a size similar to that of the engineering component [23].

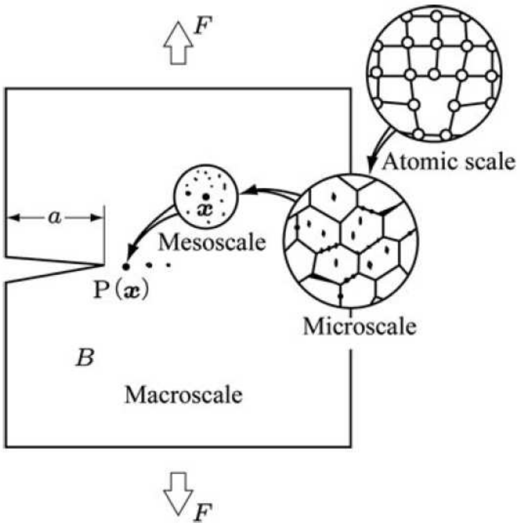

Figure 2.4.: Schematic overview for the different scales of damage processes [23].

- **Atomic scale:**
  This is the scale where damage formation has its origin, vacancies are created by splitting atomic bonds. Since the elastic properties of a material result from these bonds, it is obvious that damage formation results in stiffness reduction. Studying the material's behavior on this scale is covered in materials science [17].
- **Microscale:**
  The material appears to be heterogeneous on this scale, comprised of homogeneous sub-regions. Microcracks and microvoids are typical forms of damage observed at this scale. The growth of these defects can be studied by means of micromechanical methods [17].
- **Mesoscale:**
  A homogeneous microstructure that can be described with averaged material parameters is the characterizing trait of the mesoscale, at which the continuum constitutive equations are formulated. On the mesoscale, damage manifests itself as reduced stiffness and load-bearing ability [17]. A typical method for analyzing problems at this scale is continuum damage mechanics.
- **Macroscale:**
  The final scale relevant in damage and fracture simulations is the macroscale, which represents the size of engineering structures. The component size plays an important role in fracture processes of brittle and quasi-brittle materials due to the size-effect. Larger components have more stored elastic energy and therefore a higher damage driving potential, since the elastic energy released during crack extension must be dissipated. If the elastically released energy exceeds the energy needed for fracture, unstable crack growth takes place.

2.3. Numerical Damage and Fracture Models

Material models for the simulation of damage and fracture can be separated into three main approaches shown in figure 2.5. The distinction is based on the method of material description (continuum based or discrete) and on the way how

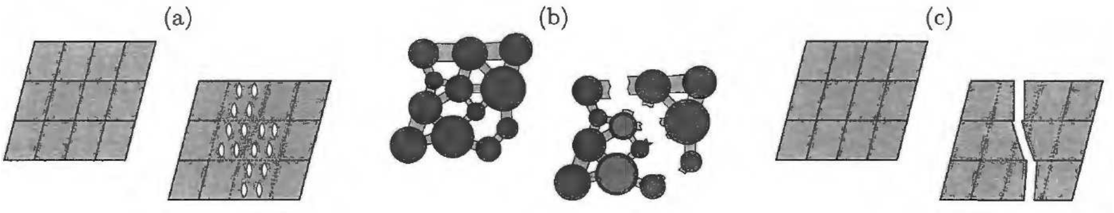

Figure 2.5.: Types of numerical damage models. (a) pure-continuum based models, (b) discrete models, (c) discontinuity-enhanced continuum models [20].

cracks are modeled (smeared or as displacement jump). The three groups are pure continuum models, discontinuity enhanced continuum models, and discrete models [20] [24]. Both groups of continuum based models rely on stress-strain relations for the material behavior, but the discontinuity-enhanced models additionally incorporate a displacement jump, which represents the separation of fracture surfaces [20]. The discrete models on the other hand do not rely on a continuum mechanics based material description, instead separate material points are linked by connections with certain elastic properties.

2.3.1. Pure continuum-based models

Pure continuum-based models assume that the damaged material is still continuous and that it can be described with a continuous displacement field. The mechanical behavior is defined by constitutive equations using average material properties homogenized over a certain volume region [29] [27]. This continuum-mechanical description is contrary to the discontinuous physical nature of defects such as microcracks, which highlights that damage is treated in a smeared sense. While some information such as the exact local strain is lost in the homogenization process, the averaged description is still suitable in many cases. The primary shortcoming of these continuum based smeared crack models is their pathological sensitivity to the mesh-size and orientation if no counter measures are taken [21] [8]. This dependency is caused by the loss of ellipticity of the governing differential equations, which results in an ill-posed problem in the sense that there is an infinite number of possible solutions [27] [24]. These issues and available remedies are further addressed in sections 3.4 and 3.5. Typical examples for pure continuum models are the smeared crack approach, continuum damage mechanics based damage models and the crack band model, which are outlined in the following.

Continuum Damage Mechanics based Models

Continuum damage mechanics is a field of science aiming at representing and predicting damage on the mesoscale, without the need to describe the responsible micromechanical mechanisms. It is easily implemented within the finite element method and represents an efficient predictive tool for damage simulations of all kind [17]. By using mechanical damage variables, different degrees of anisotropic behavior can be simulated. For a more detailed description see chapter 3.

Smeared Crack Approach

The smeared crack approach (SCA) approximates damage and fracture in a smeared sense. It was introduced in the 1960s as a counterpart to the already existing discrete crack approach for simulating damage in concrete [24] [36] [8] [25] [27] [16]. This concept is well suited for situations where dispersed cracking leads to strain-softening behavior, as is the case for concrete and ceramics [16]. The good compatibility with the standard finite element method makes these models easy to implement, which contributed to their popularity [36] [37] [16] [8]. An additional advantage compared to early versions of the discrete crack approach is that the crack-orientation can be independent of the mesh. In order to account for the damage induced anisotropy, the initially isotropic material behavior gets replaced by an orthotropic constitutive law upon crack formation [16] [27] [37]. The SCA can be divided in fixed- and rotating-crack versions, depending if the crack normal remains fixed or rotates along with the principal stress respectively [16]. It should be noted though, that the smeared crack approach can be regarded as a special case of continuum damage mechanics based models with a specific type of anisotropic behavior described by a fourth-order damage tensor [32] [25] [37].

Crack Band Model

The CDM and SCA models describe damage in a smeared sense and both suffer from mesh-size sensitivity, which can be alleviated by including the specific fracture energy and element size in the constitutive equations. Based on these two parameters, the softening-branch slope is adjusted to ensure mesh-independent energy release rate upon macrocrack formation. This remedy was initially introduced by Hillerborg for the discrete crack models [24], and was later adapted for the smeared crack approach by Bazant and Oh [37] in 1983. The resulting models with restored objectivity are called crack band models [8] [24] [25] [21]. However, while mesh-size sensitivity can be avoided, the mesh orientation dependence cannot be alleviated that way [8]. For further explanations see section 3.5.2.

2.3.2. Discontinuity Enhanced Continuum Based Models

In contrast to pure continuum approaches, the discontinuity enhanced models do not need to describe damage in a smeared sense, because the crack is modeled as a geometric entity in addition to the continuous description of the bulk material. This approach is closer to the physical problem when single macroscopic cracks are treated, where the fracture surface separation is governed by a traction-separation law [15]. Typical examples for the discontinuity-enhanced continuum models are the discrete crack approach and the extended finite element method (XFEM).

Discrete Crack Approach

The discrete crack approach has been developed in the 1960s as a method for numerical modeling of fracture in concrete. It is used to simulate the initiation and propagation of single dominant cracks, which are modeled in form of geometric discontinuities in-between continuous elements. Crack growth is assumed to occur if the nodal forces exceed a certain limit, which leads to nodal separation described by a cohesive law [24] [27]. This intuitively appealing approach, however, has some major drawbacks [27]. First of all, the discrete description does not fit the nature of continuum mechanics based standard finite element methods, which makes the implementation more difficult [16]. Secondly, cracks can only be initiated with a fixed orientation, defined by the element edges [8]. Despite the listed downsides, this approach works well in cases where the location of crack formation is known a priori, such as in the delamination of layered composites [26]. Nevertheless, these issues sparked the development of a new method called extended finite element method (XFEM) [16] [24] [27], which avoids some of the mentioned problems.

The eXtended Finite Element Method (XFEM)

Developed in the late 1990s, the extended finite element method is used to model the initiation and propagation of discontinuities, such as cracks. XFEM enriches the classical finite element method with discontinuous interpolation functions, which allows the calculation of solutions containing displacement jumps [20]. The application of this method for numerical fracture analysis bears the advantage that re-meshing is not required for an accurate description of the fracture process.

2.3.3. Discrete Models

Discrete models do not rely on a continuum mechanics based material description, instead separate material points are linked by connections with certain elastic properties. These links can either represent entire structure components such as a lattice member in a framework, or they can be used to replicate the microstructure of a material. The latter approach is used to describe the behavior of heterogeneous materials by applying the elastic connection properties correspondingly to the different phases [20]. A prominent example for a model of this group is the lattice discrete particle model developed for simulating damage and fracture in concrete.

3. Continuum Damage Mechanics

The concept of continuum damage mechanics (CDM) has been introduced by Kachanov [19] in 1958. He represents creep damage with a scalar variable, which he called integrity [17] [23]. Based on Kachanov's work, Rabotnov [35] suggested a modified definition in 1969, by introducing a so-called damage variable [23]. While this parameter is zero for a intact material, it asymptotically attains the value of one for a fully damaged material. Rabotnov also gave a meaningful physical interpretation for the damage variable parameter, by relating the reduction in load-bearing area due to defects to the initial area [17]. This Kachanov-Rabotnov theory is the prototype of CDM developed thereafter [23].

Continuum damage mechanics is a constitutive theory that describes the influence of damage on the mechanical behavior with so-called damage variables. Depending on the intended degree of anisotropy resulting from the damage formulation, the damage variable can be either a scalar or even a higher-order tensor. CDM is used to simulate the progressive loss of material integrity due to the nucleation, propagation, and coalescence of microcracks and similar defects [3]. Furthermore, this method can describe the degradation of stiffness observed on the macroscale [20], and simulate the propagation of macrocracks up to final rupture. In the context of a finite element analysis, such a crack is represented by a region of completely failed elements, which have entirely lost their stiffness and load-bearing ability [23]. The objective of CDM is the representation, modeling, and prediction of damage on the mesoscale, without the need to describe the relevant damage mechanisms on a microscopic scale [3]. This makes the continuum approximation computationally efficient and enables damage simulations of large structures [17].

Since CDM models describe the damaged material with continuum-mechanical stress-strain relations, the damage has to be regarded as smeared over a certain volume region. While some information is lost in such an averaged description, the advantage of good compatibility with the standard finite element method often justifies this simplification. However, the local simulation approach for damage and fracture by means of CDM and FEM leads to several difficulties, such as numerical-instability and mesh-sensitivity. To address these issues, several approaches called regularization techniques have been developed [23].

3.1. Mechanical Representation of Damage with Damage Variables

The material state is represented by properly defined damage variables, which can be physically interpreted either as the reduction of load-bearing area or the degradation of elastic moduli [23]. The damage variables are governed by an initiation criterion and an evolution law, which can be based on micromechanical or phenomenological considerations. While the first approach is closer to the actual physical mechanisms involved and is capable of replicating the major trends in the mechanical response, it is also more complicated and numerically demanding. Phenomenological models on the other hand are much simpler as they are based on macroscopic observations, but they cannot reflect the actual physical damage mechanisms. They are defined in such a manner that they can fit a certain stress-strain curve, either directly by a predefined diagram or via thermodynamic considerations including dissipation potentials. Since phenomenological models do not allow to incorporate the actual damage mechanisms acting on the microstructure, they have to rely on intuition and interpretation of experimentally observed trends. The choice between both approaches is a typical problem encountered when formulating a constitutive theory, where a trade-off between proper physical description and simplicity has to be made. However, for most engineering purposes it is sufficient to have an applicable predictive tool that delivers results with acceptable accuracy. Therefore, phenomenological models are predominantly found in published literature [17]. The dimension of damage variables can range from a scalar valued variable to a higher-order tensor, depending on the degree of anisotropy introduced by damage [23].

3.1.1. Scalar Damage Variable

Very basic models use a single scalar damage variable to describe isotropic damage states, which are characterized by a random distribution and orientation of spherical microvoids. It should be noted though, that a general isotropic damage model should incorporate two scalar variables, one for each of the two independent elastic moduli [20]. Otherwise the Poisson ratio remains unaffected by damage formation [23] [20]. The mathematical expression for the damage variable can be given as

$$D = \frac{A_0 - A_{\text{eff}}}{A_0} \tag{3.1a}$$

$$D = 1 - \frac{E_{\text{D}}}{E_0} \tag{3.1b}$$

where A_0 and A_{eff} are the initial and effective area, and where E_0 and E_{D} are the initial and damaged Young's modulus. Thus the damage variable D can be physically interpreted either as the reduction in load-bearing area or as the change in Young's modulus [23]. The experimental identification for the first interpretation can be done with methods such as synchrotron X-ray tomography, whereas the Young's modulus can be obtained from a simple uniaxial test. Therefore, the change in slope of a stress-strain diagram is a simple but clear indicator for material damage [17] [14].

A very appealing advantage of isotropic damage models is that the constitutive relations only get scaled by a scalar valued function upon damage formation. Thus the elasticity tensor is simply a scalar multiple of the initial undamaged one [20]. However, if the material shows pronounced anisotropic behavior, the scalar representation is in general insufficient. Nevertheless, the simplicity of a scalar model justifies its application, even for anisotropic behavior. For example in cases with proportional loading, where load reversals are not of interest, these models can still yield reliable results [23].

3.1.2. Vectorial Damage Variable

Since damage predominantly forms under tensile stress, it seems obvious that the reduction of load-bearing area should be linked to the principal stress direction. With the use of a vectorial definition of the damage variable, the damage effect can be described in three spatial directions independently corresponding to orthotropic behavior. However, the application of a vector model is more complicated than the use of a 2nd-order tensor version, which can represent orthotropic damage as well [17]. Therefore, this description is not applied very often.

3.1.3. Second-Order Tensor Damage Variable

A damage variable in the form of a symmetric 2nd-order tensor is a convenient way to incorporate anisotropic behavior, because its application is significantly simpler compared to higher-order tensors. Furthermore, the measurement of relevant material parameters for the experimental damage evaluation is not yet too cumbersome. However, 2nd-order tensors cannot describe damage more complex than orthotropy [17] [23]. Nevertheless, the assumption of damage-induced orthotropy can be a reasonable choice if anisotropic behavior cannot be neglected but the effort of higher-order tensors is to be avoided, even in cases of brittle and quasi-brittle failure more complex than orthotropy [23]. While the damage tensor itself is symmetric, the effective stress tensor is generally asymmetric, which is very inconvenient [23].

3.1.4. Fourth- and Eight-Order Tensor Damage Variable

An accurate description of pronounced anisotropic behavior such as damage in brittle and quasi-brittle materials, requires at least a 4th-order tensor damage variable [17] [23], which results in a much more complex application of these models. Furthermore, these 4th-order tensors are in general unsymmetric, which again contributes to the model complexity [23]. This issue can be avoided if symmetric 8th-order tensors are used, which map the initial stiffness tensor onto the damaged one [17] [23]. However, the increase in complexity and computational effort is very objectionable, leading to the situation where these models are only applied if they absolutely must.

3.2. Uniaxial Damage Model

In the following Section, the basics of CDM will be explained in terms of a uniaxial damage model. Let us assume a material idealized as a bundle of parallel perfectly brittle fibers, shown in Figure 3.1, which behave linear elastic until their tensile strength is reached, whereupon they break immediately. Furthermore, we assume that each fiber has a slightly different tensile strength. In a displacement controlled experiment, this simple setting leads to a situation where the load-bearing area decreases gradually beyond a certain applied displacement value. Since each fiber can be regarded as an elastic spring, the macroscopic strength and stiffness of the entire bundle decrease whenever a fiber breaks [3]. This simple illustration highlights two of the most important effects of damage formation and can be regarded as example-problem for cases with strain-softening behavior, which is typical for quasi-brittle materials.

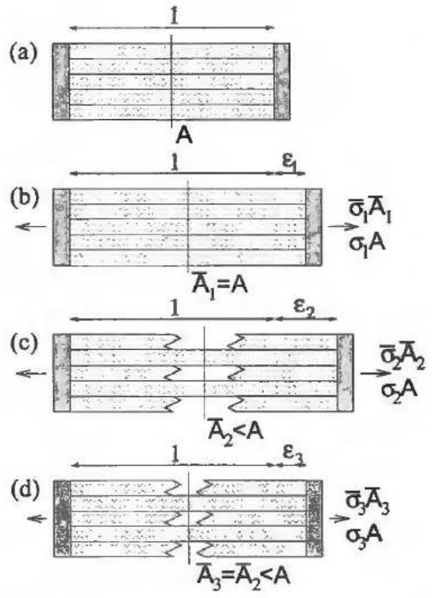

Figure 3.1.: Representation of a Uniaxial Damage Model [20].

While the fiber failure can be regarded as an example for any possible damage mechanism, the CDM modeling approach does not incorporate such processes. In the context of a finite element analysis damage is considered smeared over the entire bundle of fibers, which can be described with continuum mechanics and averaged material properties.

3.2.1. Effective Stress Notion

The reduction of load-bearing area upon fiber failure shown in Figure 3.1 makes it obvious that a distinction has to be made, between the macroscopic nominal stress

$$\sigma = \frac{F}{A_0} \tag{3.2}$$

and the effective stress

$$\sigma_{\text{eff}} = \frac{F}{A_{\text{eff}}} \tag{3.3}$$

acting on the still intact effective area, where F is the force transmitted across the fiber bundle. While the latter describes the mechanical response of the not yet damaged material, the nominal stress enters the Cauchy equations of equilibrium on the macroscopic level used in a finite element analysis. From this consideration, the stress magnifying effect of damage can be clearly seen, as the effective stress is increased over the nominal one depending on the size of the effective area.

From the equilibrium of forces

$$\sigma \cdot A_0 = \sigma_{\text{eff}} \cdot A_{\text{eff}} \tag{3.4}$$

and the damage variable definition according to equation (3.1a) follows

$$\sigma = \frac{A_{\text{eff}}}{A_0} \cdot \sigma_{\text{eff}} = \left(1 - \left[1 - \frac{A_{\text{eff}}}{A_0}\right]\right) \cdot \sigma_{\text{eff}} = (1 - D) \cdot \sigma_{\text{eff}} \tag{3.5}$$

which relates the nominal to the effective stress [14]. This equation highlights that the nominal stress is lower than the effective stress and that this difference increases if the damage variable parameter grows towards its final value $D \to 1$.

3.2.2. Strain Equivalence Principle

In order to use the stress definition according to equation (3.5), an expression for the effective stress σ_{eff} is required. This can be achieved by applying the strain equivalence principle introduced by Lemaitre [18] [23] [20].

> ***Strain Equivalence Principle:*** *Any strain constitutive equation for a damaged material may be derived in the same way as for a virgin material except that the usual stress is replaced by the effective stress.*

This principle allows for a simple definition of the effective stress in damaged materials by replacing the nominal stress in the constitutive equations for the undamaged material. In the current uniaxial case, this corresponds to $\sigma_{\text{eff}} = E_0 \cdot \varepsilon$ [14]. By incorporating this relation into equation (3.5) we get the homogenized constitutive law on the macroscopic level

$$\sigma = (1 - D) \cdot E_0 \cdot \varepsilon \tag{3.6}$$

which relates the nominal stress to the strain and the damage variable, and is used in a FEM simulation. Furthermore, this relation makes it obvious that a damaged material responses with reduced stiffness

$$E_D = (1 - D) \cdot E_0 \tag{3.7}$$

compared to the undamaged situation [14].

3.2.3. Damage Growth Criterion and Evolution Law

To complete the uniaxial damage model, a criterion specifying the onset of damage growth and an evolution law describing the progressive increase of the damage variable D are needed. For the sake of simplicity, damage evolution is assumed to be exclusively strain driven. This assumption is justified for the tensile strain driven microcrack formation in brittle and quasi-brittle materials [23]. However, since damage cannot decrease the evolution function must be evaluated with the largest previously reached strain value at time t

$$\kappa(t) = \max_{\tau \leq t} (\varepsilon_0, \varepsilon(\tau)) \tag{3.8}$$

where ε_0 is the strain value at the materials tensile strength, representing the initial damage onset threshold and $\varepsilon(\tau)$ is the strain history. With this definition, damage simulations are not restricted to cases of monotonic loading. The onset of damage growth is detected with the simple criterion

$$\varepsilon > \kappa \tag{3.9}$$

which states that damage will grow whenever the current strain exceeds its previously largest value, whereupon κ is updated. The extent of damage growth can be obtained by comparing the damaged and initial stiffness according to equation (3.1b). Therefore, the shape of the post-peak stress-strain behavior determines the damage evolution function

$$D = D(\kappa) \tag{3.10}$$

which is defined as function of κ.

3.3. Isotropic Damage Model

The simplest model for general stress-states can be obtained by extending the uniaxial version from the previous Section, which leads to an isotropic model with a single damage variable. Based on equation (3.6), the scalar stress, strain, and Young's modulus are replaced with their tensor-valued counterparts, which leads to

$$\underset{\sim}{\sigma} = (1 - D) \cdot \underset{\approx}{\mathbb{E}}^0 : \underset{\sim}{\varepsilon} \tag{3.11}$$

where $\underset{\sim}{\sigma}$ and $\underset{\sim}{\varepsilon}$ are the stress and strain tensors and where $\underset{\approx}{\mathbb{E}}^0$ represents the initial undamaged elasticity tensor of an isotropic material. Although the assumption of isotropy is obviously not fulfilled in most damaged materials, as described in Section 2.2.3, the simplicity and ease of implementation often justifies their application. The most appealing property of isotropic damage models is that the damaged elasticity tensor is merely a scalar multiple of the initial intact case [21].

3.3.1. Equivalent Strain

Calculation of the damage variable for general strain states requires the definition of a scalar measure from the strain tensor $\underset{\approx}{\varepsilon}$, which is called equivalent strain, $\varepsilon_{\mathrm{equ}}$, [20] [21]. With the use of this scalar measure for the strain state, it is possible to use the damage growth criterion and damage evolution law defined by the equations (3.9) and (3.10) in the form of

$$\varepsilon_{\mathrm{equ}} > \kappa \tag{3.12a}$$

$$D = D(\kappa) \tag{3.12b}$$

where κ is now the largest previously reached equivalent strain value

$$\kappa(t) = \max_{\tau \leq t} \left(\varepsilon_0, \varepsilon_{\mathrm{equ}}(\tau)\right) \tag{3.13}$$

at time t. Different methods for the calculation of the equivalent strain are published in [20], some of which are introduced in the following. The euclidean norm

$$\varepsilon_{\mathrm{equ\_EuclideanNorm}} = \sqrt{\underset{\approx}{\varepsilon} : \underset{\approx}{\varepsilon}} = \sqrt{\varepsilon_{ij}\varepsilon_{ij}} \tag{3.14}$$

and the energy norm

$$\varepsilon_{\mathrm{equ\_EnergyNorm}} = \sqrt{\frac{\underset{\approx}{\varepsilon} : \underset{\approx}{\mathbb{E}}^0 : \underset{\approx}{\varepsilon}}{E_0}} = \sqrt{\frac{1}{E_0}\varepsilon_{ij}\mathbb{E}^0_{ijkl}\varepsilon_{kl}} \tag{3.15}$$

represent two very simple definitions for the equivalent strain. In cases where tensile loads are the dominant cause for microcrack formation such as in concrete, the different behavior in tension and compression can be considered by neglecting the negative part of the strain tensor. This leads to the so-called Mazars definition for the euclidean norm

$$\varepsilon_{\mathrm{equ\_MazarsEuclideanNorm}} = \sqrt{< \underset{\approx}{\varepsilon} >:< \underset{\approx}{\varepsilon} >} \tag{3.16}$$

and for the energy norm, also called energy norm of positive strain,

$$\varepsilon_{\text{equ\_MazarsEnergyNorm}} = \sqrt{\frac{<\underset{\sim}{\varepsilon}>: \underset{\approx}{\mathbb{E}}^{0} :<\underset{\sim}{\varepsilon}>}{E_0}} \tag{3.17}$$

which use Macauley brackets $< x >= \max(0, x)$ to obtain the positive part of the strain tensor [20]. With this mathematical operator, the positive part of the symmetric strain tensor is obtained by

$$<\underset{\sim}{\varepsilon}>= \sum_{I=1}^{3} < \varepsilon_I > \boldsymbol{n}_I \otimes \boldsymbol{n}_I \tag{3.18}$$

where ε_I are the principal strains and $\boldsymbol{n}_I$ are the principal direction vectors [20]. However, the damage behavior cannot be regarded as isotropic anymore if equations (3.16) or (3.17) are used for the equivalent strain.

In order to demonstrate how the equivalent strain definition influences the elastic domain, Figure 3.2 is given, which shows a plane-stress loading state projected onto the normalized principal strain plane. As can be seen, the euclidean norm and energy norm are both elliptical and symmetric with respect to the origin, which highlights that there is no distinction between the tensile and compressive behavior [20]. The Mazars definition and the energy norm of positive strain on the other hand show an extended elastic domain in the compressive region, which corresponds to a material behavior with a higher compressive than tensile strength.

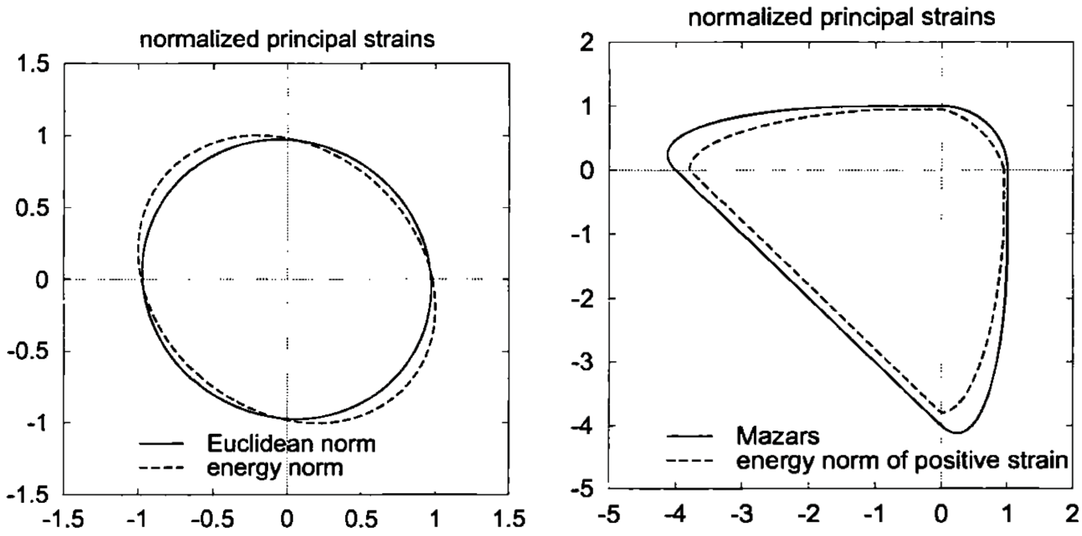

(a) Euclidean norm and energy norm.

(b) Mazars definition and energy norm of positive strain.

Figure 3.2.: Elastic domains corresponding to different equivalent strain definitions for a plane-stress loading state projected onto the normalized principal strain space [20].

3.4. Common Issues encountered in Strain-Softening Materials

The continuum damage mechanics approach is simple to implement within the standard finite element method and can be used for a wide range of fracture problems. However, the combination of CDM and FEM also leads to a number of problems when applied to strain-softening materials, which are characterized by decreasing material strength when the strains are increased beyond the elastic limit as explained in section 2.2.2. Typical issues are strain localization widths that do not correspond to experimental observations, numerical instability and mesh-sensitivity, which have been addressed by several approaches developed in the past [23]. Numerical instability and mesh-dependence are crucial problems in the application of CDM within the finite element method and must be solved in any case to get applicable results [23]. Strain localization into element bands with a width that does not correspond to physical observations on the other hand is accepted in many cases, if the dissipation results are reasonable.

3.4.1. Material Instability and Strain-Localization

Material instability in the form of strain-softening leads to strain-localization in a region as narrow as possible. In a FEM analysis this usually corresponds to a band with almost mesh-size width [23] [17] [14]. The actual experimentally observed width of the localization band, which seems to be a material constant, is not reproduced in numerical CDM simulations, except when further measures are taken.

At continuum level, a stable material behavior is characterized by Hill's stability criterion

$$\underset{\sim}{\dot{\varepsilon}}^{\mathrm{T}} : \underset{\sim}{\dot{\sigma}} > 0 \tag{3.19}$$

which requires that the scalar product between the stress rate and strain rate tensors is positive [28]. Inserting equation (3.19) into the constitutive law in rate form

$$\underset{\sim}{\dot{\sigma}} = \underset{\approx}{\mathbb{E}}^{\mathrm{t}} : \underset{\sim}{\dot{\varepsilon}} \tag{3.20}$$

where $\underset{\approx}{\mathbb{E}}^{\mathrm{t}}$ is the material tangential stiffness tensor, we obtain

$$\underset{\sim}{\dot{\varepsilon}}^{\mathrm{T}} : \underset{\approx}{\mathbb{E}}^{\mathrm{t}} : \underset{\sim}{\dot{\varepsilon}} > 0 \tag{3.21}$$

which is only fulfilled if the material tangential stiffness tensor is positive definite [28]. This is the case if the condition

$$\det(\underset{\approx}{\mathbb{E}}^{\mathrm{t}}) > 0 \tag{3.22}$$

for the determinant is satisfied [28]. Equation (3.22) represents a simple criterion for material stability, which is obviously not fulfilled for materials that exhibit strain-softening due to the negative slope in the stress-strain diagram.

The problems of such an unstable material behavior are that it can lead to structural instability and that it causes issues such as mesh-size sensitivity and numerical instability [23]. These issues are caused by the loss of ellipticity of the governing rate equations, which leads to an ill-posed problem. Results with elliptic character do not allow the existence of discontinuities in the solution field, thus problems with strain-localization cease to be elliptic.

3.4.2. Mesh-Sensitivity

The fact that strain localizes in a region as narrow as possible in strain-softening materials leads to pronounced mesh-sensitivity of the results as the crack width is governed by the mesh. Furthermore, the amount of dissipated energy is linked to the volume of failed elements, thus a reduction in mesh-size also leads to reduced dissipation [23]. This non-objective behavior and the issue of vanishing energy dissipation upon mesh-refinement must be prohibited in order to obtain meaningful results [23]. Several approaches such as mesh-adjusted softening or non-local damage models have been developed for addressing these problems.

To illustrate mesh-sensitivity of numerical results one can consider a simple bar under uniaxial tension, simulated with different mesh resolutions. As can be seen in Figure 3.3, the softening slope in the load-displacement diagram gets steeper with an increasing number of elements. The slope even bends backwards for a sufficiently fine discretization, which corresponds to snap-back behavior. The observed trend can be explained with the reduced amount of dissipation, represented by the area under the curve, when damage localizes in smaller elements.

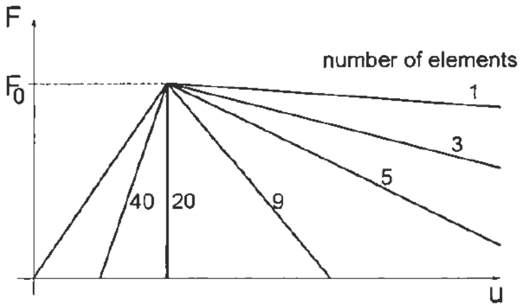

Figure 3.3.: Load-displacement diagram of a bar under uniaxial tension representing mesh-sensitivity. Strain localization takes place into a single element. [20]

3.4.3. Numerical Instability

The ill-posed boundary value problem, resulting from a non-positive definite tangent stiffness tensor, exhibits non-unique solutions [23]. Therefore the numerical algorithms implemented in commercial software packages struggle to get a converging solution. Furthermore, the transition from a uniform displacement field to a localized one takes place in just a single incremental calculation step, thus the solver has difficulties due to this sudden change in the elastic behavior.

3.5. Regularization Techniques

The typical issues encountered in a continuum damage mechanics based simulation of strain-softening materials, which have been described in the prior section, have led researchers to develop numerous approaches for their remedy. Some of these methods are absolutely necessary in order to obtain reasonable results, such as ensuring numerical stability and objectivity [14]. Without these traits, simulations would not converge and results would strongly depend on the spatial discretization. Other methods even address the issue of localization band width by adding an additional length parameter to the simulation, which prevents that damage and strain localize in smaller regions than the added characteristic length. This is the group of so-called non-local damage models, which present the most promising approach for treating strain-softening materials. However, compared to purely local approaches these models are more complicated and require additional computational effort.

3.5.1. Artificial Viscosity or Viscous Regularization

Quasi-brittle materials exhibiting strain-softening behavior show pronounced convergence difficulties in implicit analyses, which can be improved by using viscous regularization [7] [15]. Adding an artificial viscosity term helps the numerical algorithms to obtain converged solutions, as the positive-definiteness of the tangent stiffness matrix can be restored for sufficiently small time increments [7] [23]. This is achieved by slowing down the damage growth rate, which results in a slowed down change for the displacement field [7]. Otherwise the transition from a rather uniform to a localized field would be very sudden, which is difficult for the numerical algorithms to reproduce.

The implementation of artificial viscosity is done by replacing the original inviscid damage variable D in the constitutive equations with the newly defined viscous damage variable D_v, which is governed by the rate equation

$$\dot{D}_\mathrm{v} = \frac{1}{\eta}(D - D_\mathrm{v}) \tag{3.23}$$

where η is the artificial viscosity coefficient that represents the relaxation time [7] [15]. Usually small values compared to the characteristic time increment already help to improve the convergence rate without affecting the results too much [7]. Due to the rate equation definition, the viscous solution is relaxing towards the inviscid one for $t \to \infty$ [7]. However, viscous regularization also causes an increased fracture energy for higher deformation rates, which has to be considered in the simulation [7].

3.5.2. Mesh-Adjusted Softening

Since the amount of dissipated energy depends by the volume of failed elements, the mesh-size has a major impact on the numerical results in strain-localization problems. To ensure a mesh-independent fracture energy, methods such as mesh-adjusted softening have been developed, which are inspired by the cohesive crack model introduced by Hillerborg [1] and the crack band model introduced by Bazant and Oh [37]. The method is based on an objective stress-displacement material description shown in Figure 3.4 (a), where the amount of dissipation is defined by the fracture energy per unit area G_f, which is a material constant [5]. The characteristic element length l^e is used to scale the area under the corresponding stress-strain diagram shown in Figure 3.4 (b), such that the volumetric dissipation $g_\mathrm{f} = G_\mathrm{f}/l^\mathrm{e}$ depends on the element size [4] [21]. Therefore, the softening slope of the stress-strain diagram is adjusted in dependence of the characteristic length as can be seen in Figure 3.5. This means that smaller elements have a higher volumetric dissipation in order to obtain objective results [23] [4].

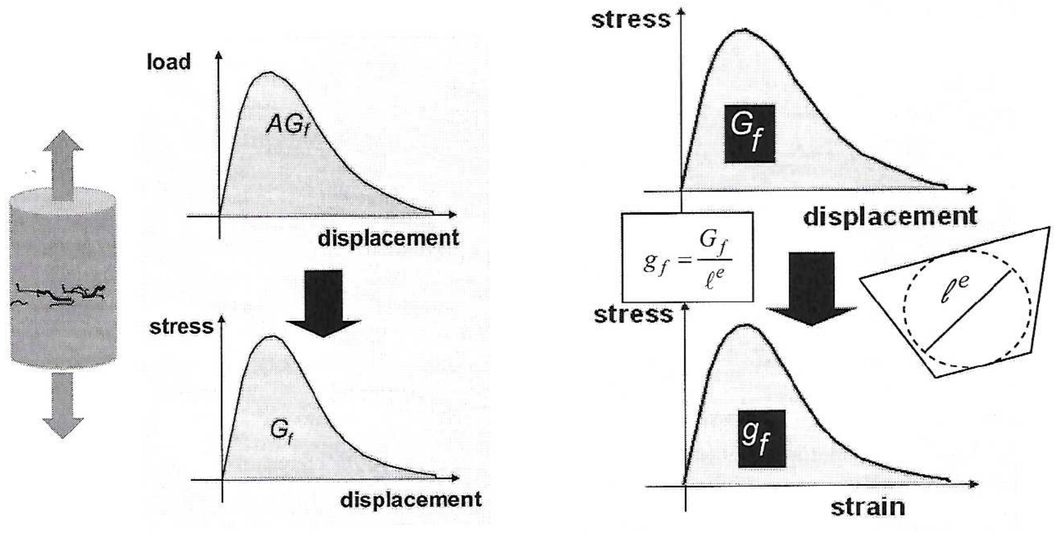

(a) Representation of the fracture energy. (b) Fracture energy regularization using the characteristic element length l^e.

Figure 3.4.: Fracture energy regularized stress-strain diagram obtained from am objective load-displacement relation [4].

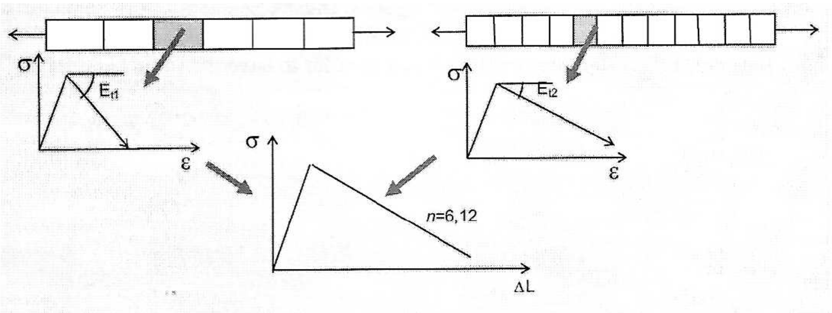

Figure 3.5.: Representation of the mesh-adjusted softening method [4].

The nonphysical vanishing dissipation upon mesh-refinement can be avoided and objectivity of the numerical results may be restored with this method [23] [4]. However, the issue that the numerical strain localization width does not correspond to physical observations cannot be addressed. The method is based on the assumption that strain and damage localize in a one element thick layer. Therefore, objectivity of the results is not restored in general but only in cases that fulfill this assumption [4]. While the definition of mesh-size dependent material properties is questionable from a physical point of view [23], it still represents a simple and effective regularization technique whose application is justified.

3.5.3. Non-Local Damage Theory

If the simulation shall replicate the experimentally observed fracture process zone width, which is assumed to be a material constant [16] [37] [38], then it is necessary to implement a localization limiter [11]. This is done in non-local damage models, which regularize the amount of dissipated energy by numerically reproducing the experimentally observed localization width. These models enforce damage to spread over several elements up to a width equal to the characteristic length. Therefore objectivity is restored and additionally a realistic prediction for the damaged volumes size is given [21]. The damage state at a certain point $P(\vec{x})$ not just evaluated locally, but also in dependence of the surrounding region up to a certain distance specified by the characteristic length. The averaged non-local damage variable then replaces the local counterpart in the constitutive and evolution equation [23]. However, these methods require additional modeling and numerical effort compared to purely local models [21].

Non-Local Integral Damage

The non-local integral damage approach is one of the most rational and effective schemes available for suppressing strain-localization into smaller regions than the physically observed width. Therefore this method has been widely applied in CDM analyses of quasi-brittle materials with strain-softening behavior [23]. The calculation of non-local variables $\bar{A}$ includes the values at surrounding nodes in a weighted form. They are defined by the equation

$$\bar{A}(\vec{x}) = \frac{1}{V} \int_V h(\vec{s} - \vec{x}) \cdot A(\vec{s}) dV(\vec{s}) \tag{3.24}$$

where $A(\vec{x})$ is the local variable and $h(\vec{x})$ is a weighting function. Typically the Gaussian distribution $h(\vec{x}) = \exp(-\frac{|\vec{x}|^2}{2l^2})$ is used, where l is the characteristic length [23].

Non-Local Gradient-Dependent Theory

The obvious counterpart to integral based approaches is the gradient-dependent theory, which defines a non-local variable $\bar{A}$ as a function of the local variables gradient $\nabla A(\vec{x})$ [23].

$$\bar{A}(\vec{x}) = A(\vec{x}) + c_1 \nabla A(\vec{x}) + c_2 \nabla^2 A(\vec{x}) + \ldots \tag{3.25}$$

However, the gradient based approach is numerically more complicated than the integral non-local method [23].

4. Modeling Approach

The chosen isotropic CDM modeling approach for the elasto-damage constitutive model is implemented in Abaqus/Standard 2018, a simulation environment by Dassault Systèmes (Vélizy-Villacoublay, France). It provides an interface that can be used to implement a user-defined mechanical constitutive behavior with a so-called UMAT-subroutine. In the following sections, a short overview of the finite element method is given and the implemented damage model is discussed in detail.

4.1. Finite Element Method

The Finite Element Method (FEM) is one of the most widely used numerical methods for solving boundary value problems (BVPs) which are described by a set of partial differential equations (PDEs). It is commonly used in structural analysis, heat transfer simulations, and many other applications. The underlying principle that all numerical methods have in common is the discretization, which reduces the continuous problem into one with a finite number of degrees of freedom (DOFs). Therefore the set of PDEs is transformed into a system of algebraic equations, which can be solved numerically. The displacement field gets calculated at the nodes and is interpolated in-between. A key feature of the FEM is its space discretization into finite elements, which leads to simple interpolation functions. Typically first or second order polynomials are used, corresponding to linear- and quadratic-elements. Equilibrium equations are defined for every element in terms of nodal force, displacement, and stiffness. The global system of equations

$$\underline{\underline{M}}\,\underline{\ddot{u}} + \underline{\underline{C}}\,\underline{\dot{u}} + \underline{\underline{K}}\,\underline{u} = \underline{F} \tag{4.1}$$

is obtained by assembling all element contributions where $\underline{\underline{M}}$, $\underline{\underline{C}}$, $\underline{\underline{K}}$ are the mass-, damping-, and stiffness-matrix, and $\underline{\ddot{u}}$, $\underline{\dot{u}}$, $\underline{u}$, $\underline{F}$ are the vectors of nodal acceleration, velocity, displacement, and force [30]. Depending on the problem, inertia effects and therefore acceleration may be negligible. In these cases the simulation can be assumed as quasi-static.

4.1.1. Linear and Non-Linear Simulation

Although physical problems are often nonlinear, in many cases the effects of non-linearity can be neglected and the problem linearized. This simplifies the numerical treatment to a large degree, since only a single algebraic system of equations has to be solved. In terms of static structural analyses this corresponds to the solution of

$$\underline{\underline{K}}\,\underline{u} = \underline{F} \tag{4.2}$$

where $\underline{\underline{K}}$ is the constant stiffness matrix [30]. The linearization is justified if the material behavior and boundary conditions are linear and if the deformations and strains remain small [22]. The benefits of linear simulations are that the solution is path-independent, can be obtained with a direct numerical solver and can be applied in superposition to other linear load cases [22].

In cases where the contribution of nonlinear effects is no longer insignificant, it is required to consider them during the simulation. This is done with nonlinear numerical procedures, which consider the global stiffness to be a function of the nodal displacements $\underline{\underline{K}}(\underline{u})$ [22]. The solution path is obtained by applying the load in steps, the so-called increments, which are linearized and solved numerically. Typical sources for nonlinear behavior are:

- non-linear material response [7] [22]
- geometrical nonlinearities (large deformations and/or large strains) [7] [22]
- changing boundary conditions during the simulation (e.g. contact) [7] [22]
- bifurcation of equilibria (e.g. buckling) [22]

4.1.2. Explicit and Implicit Methods

The solutions path-dependence in a nonlinear FEM simulation is obtained by applying the load in increments. These piece-wise linearized systems of equations can be solved either with explicit or implicit methods, which are briefly described in this section.

Implicit methods solve the nonlinear equation (4.1) in each increment with an iterative solver, ensuring that the obtained solution fulfills the equilibrium conditions according to a specified convergence criteria [31]. An example for such an incremental-iterative procedure is the Newton-Raphson method, which is used in Abaqus/Standard. Advantages of implicit methods are the unconditional stability and that relatively large increment sizes can be used [7] [31]. However, the computational effort per increment is high due to the iterative method and obtaining a converged solution may be challenging for certain problems [7]. Furthermore, the system of equations has to be solved simultaneously for $\underline{u}$ as the problem is coupled by the stiffness-matrix [31].

In explicit methods on the other hand, the equilibrium equations (4.1) are solved for $\underline{\ddot{u}}$ [31], where the mass-matrix is typically considered 'lumped' in the sense that it has a diagonal shape. This means that it can be easily inverted and that the problem is no longer coupled, thus it can be solved directly without the need for a simultaneous solving procedure [7] [31]. Such an explicit direct-integration scheme is used in Abaqus/Explicit. The computational effort per increment is low, but the explicit method is only conditionally stable and requires small increments [7] [31]. Depending on the problem either explicit or implicit numerical methods may be more suitable. While implicit methods are typically applied in quasi-static problems, explicit methods are better suited for highly dynamic simulations [7]. Also in certain quasi-static cases, where the implicit solver has trouble to obtain a converged solution as is the case in contact problems or complex material simulations, the explicit method may be better suited [7] [31].

4.2. Damage Model Implementation in Abaqus/Standard

The developed isotropic elasto-damage model is implemented in Abaqus/Standard 2018 by Dassault Systèmes (Vélizy-Villacoublay, France). It features mesh-adjusted softening and viscous regularization techniques in order to ensure objectivity and to obtain converging results. The constitutive model is intended for fracture and damage simulations of quasi-brittle materials such as concrete.

Abaqus/Standard is a commercial implicit FEM software package, which provides an interface that can be used to implement a user-defined mechanical constitutive behavior with a so-called UMAT-subroutine. This subroutine is a code that has to be written in FORTRAN and is executed at the integration points, where the materials stress response and the tangent stiffness matrix have to be calculated. Within the UMAT it is possible to store so-called solution-dependent state variables at each integration point, which may be used for parameters such as the damage variable and damage growth initiation threshold [7]. These solution-dependent state variables have to be initialized and it is necessary to specify their number since Abaqus has to allocate space for them. Additionally the element deletion option can be enabled, where the default value for the assigned deletion state-variable is one. Abaqus will exclude the integration point from the analysis if it set to zero and delete the entire element from the mesh once all integration points are excluded.

Tables listing the input and output variables for the developed elasto-damage model and an example Abaqus input-file are provided in the Abstract A.2 and A.3, respectively.

4.2.1. Isotropic Elasto-Damage Constitutive Model

As described in section 3.3, the constitutive equation for an isotropic damage model is given by

$$\underset{\sim}{\boldsymbol{\sigma}} = (1 - D) \cdot \underset{\approx}{\mathbb{E}}^{0} : \underset{\sim}{\boldsymbol{\varepsilon}} \tag{4.3}$$

with $\underset{\approx}{\mathbb{E}}^0$ as the initial undamaged elasticity tensor of an isotropic material. Since damage is assumed to be exclusively strain-driven in the implemented constitutive model, the damage variable D depends exclusively on the strain tensor. To account for general strain states, a scalar measure for the strain tensor called equivalent strain

$$\varepsilon_{\mathrm{equ}} = \sqrt{\frac{\underset{\sim}{\varepsilon} : \underset{\approx}{\mathbb{E}}^0 : \underset{\sim}{\varepsilon}}{E_0}} = \sqrt{\frac{1}{E_0}\varepsilon_{ij}\mathbb{E}^0_{ijkl}\varepsilon_{kl}} \tag{4.4}$$

is used, which is calculated with the energy norm. Onset of damage growth is defined by the simple initiation criterion

$$\varepsilon_{\mathrm{equ}} > \kappa \tag{4.5}$$

where κ is the largest previously reached equivalent strain with an initial value corresponding to the strain at ultimate strength. An evolution law for the damage variable in the form of $D = D(\kappa)$ is derived from the bi-linear stress-strain diagram shown in Figure 4.1 obtained for the set of material parameters and characteristic element length listed on top of the figure.

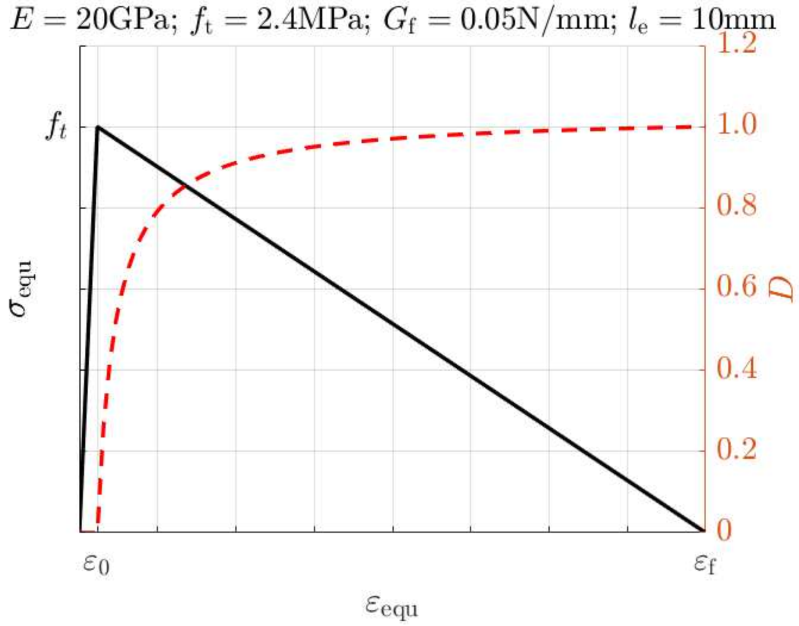

Figure 4.1.: Stress-strain diagram with linear elastic and linear strain-softening behavior and damage variable development.

The derivation is based on the consideration that the post-peak stress can be calculated as a function of the equivalent strain by one of two ways. Firstly to use the reduced stiffness

$$\sigma_{\mathrm{equ}} = (1 - D) E_0 \varepsilon_{\mathrm{equ}} \tag{4.6}$$

and secondly to use the softening-slope

$$\sigma_{\mathrm{equ}} = E_0 \varepsilon_0 - \frac{E_0 \varepsilon_0}{\varepsilon_{\mathrm{f}} - \varepsilon_0} (\varepsilon_{\mathrm{equ}} - \varepsilon_0) \tag{4.7}$$

where ε_0 and ε_{f} are the strain values at ultimate strength and total failure from a uniaxial tensile response and with E_0 as the initial undamaged Young's modulus. The following evolution function for the scalar damage variable

$$D = \frac{\varepsilon_{\mathrm{f}}(\kappa - \varepsilon_0)}{\kappa(\varepsilon_{\mathrm{f}} - \varepsilon_0)} = \frac{\varepsilon_{\mathrm{f}}}{(\varepsilon_{\mathrm{f}} - \varepsilon_0)} \left(1 - \frac{\varepsilon_0}{\kappa}\right) \tag{4.8}$$

follows from equations (4.6) and (4.7) as well as from the consideration that damage is evaluated with κ instead of the equivalent strain as described in section 3.3. Equation (4.8) shows that the damage variable grows towards the value of one $D \to 1$ when $\kappa \to \varepsilon_{\mathrm{f}}$, and finally becomes equal to one $D(\kappa = \varepsilon_{\mathrm{f}}) = 1$. Damage evolution according to this definition and the bi-linear stress response is shown in Figure 4.1, obtained for a chosen set of material parameters and characteristic element length listed on the figures top. As can be seen, damage begins to grow once the initial growth onset threshold ε_0 is exceeded. This strain value, corresponding to the ultimate strength, can be calculated from

$$\varepsilon_0 = \frac{f_{\mathrm{t}}}{E_0} \tag{4.9}$$

where f_{t} is the tensile strength. The strain at final failure ε_{f} on the other hand is not only depending on the material, but also on the used numerical mesh-size due to the mesh-adjusted softening regularization described in section 3.5.2. The implementation of this mesh-adjusted softening technique is described in the following section.

4.2.2. Implementation of Mesh-Adjusted Softening Regularization

The pronounced mesh-dependency encountered in strain-softening problems requires certain methods to restore objectivity of the numerical results, otherwise these simulations cannot provide reliable predictions. In the implemented damage model the so-called mesh-adjusted softening method is applied, which adjusts the softening-slope of the stress-strain diagram and thus the underlying material behavior. The adjustment depends on the characteristic element size l^{e} and aims at ensuring a mesh-independent energy dissipation. A theoretical treatment of this regularization technique can be found in section 3.5.2.

The fundamental principle of this method is that the volumetric energy dissipation, corresponding to the area under the stress-strain diagram, is magnified when the element size and therefore the volume of failed elements is decreased. This way the dissipated energy per crack unit area equals the fracture energy G_{f} and the total dissipated energy, corresponding to the area under the force-displacement diagram, is independent of the chosen mesh-size. However, it should be noted that this method only works when damage and strain localize into a single layer of elements, otherwise objectivity is not restored. Therefore this technique is sometimes regarded as pseudo-regularization [4].

The mathematical expression for the strain at final rupture

$$\varepsilon_{\mathrm{f}} = \frac{2 \cdot G_{\mathrm{f}}}{E \cdot \varepsilon_0 \cdot (l^{\mathrm{e}} \cdot \mathrm{CF})} \tag{4.10}$$

is derived from the aforementioned assumption that the area under the stress-strain diagram shown in Figure 4.1

$$\text{area} = \frac{1}{2} E_0 \varepsilon_0^2 + \frac{1}{2} E_0 \varepsilon_0 (\varepsilon_{\mathrm{f}} - \varepsilon_0) = \frac{1}{2} E_0 \varepsilon_f \varepsilon_0 \tag{4.11}$$

is equal to the fracture energy density

$$g_{\mathrm{f}} = \frac{G_{\mathrm{f}}}{(l^{\mathrm{e}} \cdot \mathrm{CF})} \tag{4.12}$$

obtained when the specific fracture energy is divided by the characteristic element length scaled with the correction factor CF. This correction factor can be used to compensate a possible difference between the characteristic element length and the actual width of the failed element layer. Such a deviation between these two lengths occurs for example in the case of a plane-strain triangular mesh, where the characteristic element length is smaller than the layer width formed by these elements. The characteristic element length is provided by Abaqus as CELENT parameter in the UMAT subroutine. This parameter is calculated from the square root of the element area or cubic root of the element volume for 2D and 3D elements, respectively. Therefore, the characteristic element length and actual localization width are only equal in specific cases, such as quadrilateral and hexahedral elements with an aspect ratio of one, where the elements are aligned to the crack path. It should be noted that there is an upper bound for the scaled characteristic element length, which originates from the condition

$$\varepsilon_0 < \varepsilon_{\mathrm{f}} \tag{4.13}$$

which prevents snap-back behavior on the continuum level.

4.2.3. Implementation of Viscous Regularization

As already described in section 3.4, the numerical treatment of strain-softening material behavior with implicit FEM is accompanied by numerical instability. A possible remedy is to incorporate an artificial viscosity parameter that slows down the rate of change for the damage evolution, which helps the numerical solver to obtain a converged solution. This method improves the convergence behavior without compromising the results, if the artificial viscosity parameter is chosen appropriately. A guideline for the application of viscous regularization can be found in the Abaqus online documentation [7] and in [15] [23].

This method is implemented by defining a viscous damage variable, D_{v}, which is defined by the following rate equation

$$\dot{D}_{\mathrm{v}} = \frac{1}{\eta}(D - D_{\mathrm{v}}) \tag{4.14}$$

where η is the artificial viscosity parameter. This viscous variable D_{v} then replaces the original inviscid damage variable D

$$\underset{\sim}{\boldsymbol{\sigma}} = (1 - D_{\mathrm{v}}) \cdot \underset{\approx}{\mathbb{E}}^{0} : \underset{\sim}{\boldsymbol{\varepsilon}} \tag{4.15}$$

in the constitutive equation.

For the numerical implementation, the rate equation (4.14) is discretized using the forward finite difference approach

$$\frac{D_{\mathrm{v}}^{\mathrm{n}+1} - D_{\mathrm{v}}^{\mathrm{n}}}{\Delta t} = \frac{1}{\eta}(D^{\mathrm{n}+1} - D_{\mathrm{v}}^{\mathrm{n}+1}) \tag{4.16}$$

where the indices n+1 and n represent the state at time $t + \Delta t$ and t respectively. The time increment Δt is not constant, but is adjusted by the numerical solver as required for the equilibrium iterations. From this approach it is simple to obtain an explicit evolution equation for the viscous damage variable

$$D_{\mathrm{v}}^{n+1} = \frac{D_{\mathrm{v}}^{\mathrm{n}} + (\Delta t/\eta) D^{\mathrm{n}+1}}{1 + (\Delta t/\eta)} \tag{4.17}$$

which is a weighted average of its value at the previous increment $D_{\mathrm{v}}^{\mathrm{n}}$ and the inviscid damage variable at the current increment $D^{\mathrm{n}+1}$. Furthermore, the importance of $(\Delta t/\eta)$ can be seen, because this ratio determines whether or not the growth rate of the viscous damage variable is similar to that of the inviscid one. For $(\Delta t/\eta) >> 1$ the difference between both damage variables vanishes, whereas the growth of D_{v} is slowed down for $(\Delta t/\eta) << 1$. Thus the compromising effect caused by this regularization technique increases when the ratio $(\Delta t/\eta)$ decreases.

4.2.4. Derivation of the Tangent-Stiffness Tensor

The incremental-iterative numerical solver in Abaqus/Standard requires the current tangent stiffness matrix

$$\frac{d\underset{\sim}{\boldsymbol{\sigma}}}{d\underset{\sim}{\boldsymbol{\varepsilon}}} \tag{4.18}$$

also called the material Jacobian, as output of the UMAT-subroutine. This matrix is used in the iteration process and affects only the convergence rate but not the converged results [7]. A correct definition of the consistent material Jacobian preserves the quadratic convergence rate of the Newton-Raphson method [7]. In the UMAT-subroutine the stresses and the Jacobian are not defined as tensors but as vector and matrix corresponding to the Abaqus convention [7]. Here we will refer to the actual tangential stiffness tensor as $\underset{\approx}{\mathbb{E}}^{\mathrm{t}}$ and to the tangent stiffness matrix as $\underline{\underline{\boldsymbol{E}}}^{\mathrm{t}}$.

In order to derive the tangential stiffness tensor, equation (4.15) is differentiated with respect to the strain tensor $\underset{\sim}{\boldsymbol{\varepsilon}}$

$$\underset{\approx}{\mathbb{E}}^{\mathrm{t}} = \frac{d\underset{\sim}{\boldsymbol{\sigma}}(D_{\mathrm{v}}, \underset{\sim}{\boldsymbol{\varepsilon}})}{d\underset{\sim}{\boldsymbol{\varepsilon}}} = \frac{\partial \underset{\sim}{\boldsymbol{\sigma}}}{\partial \underset{\sim}{\boldsymbol{\varepsilon}}} + \frac{\partial \underset{\sim}{\boldsymbol{\sigma}}}{\partial D_{\mathrm{v}}} \frac{\partial D_{\mathrm{v}}}{\partial \underset{\sim}{\boldsymbol{\varepsilon}}} \tag{4.19}$$

which yields a relation where the first part is always active, whereas the second part only contributes when damage grows. After the straightforward differentiation of the stress tensor with respect to the strain tensor and with respect to the viscous damage variable, this equation takes the form

$$\underset{\approx}{\mathbb{E}}^{\mathrm{t}} = (1 - D_{\mathrm{v}})\underset{\approx}{\mathbb{E}}^{0} - \frac{\partial D_{\mathrm{v}}}{\partial \underset{\sim}{\boldsymbol{\varepsilon}}} \otimes \left(\underset{\approx}{\mathbb{E}}^{0} : \underset{\sim}{\boldsymbol{\varepsilon}}\right) \tag{4.20}$$

where only the derivative of the viscous damage variable with respect to the strain tensor is undefined [20]. This derivative is obtained by using the product rule shown in equation (4.21). The separate derivatives of this product rule are shown in equations (4.22) - (4.25).

$$\frac{\partial D_{\mathrm{v}}}{\partial \underset{\sim}{\boldsymbol{\varepsilon}}} = \frac{\partial D_{\mathrm{v}}}{\partial D} \frac{\partial D}{\partial \kappa} \frac{\partial \kappa}{\partial \varepsilon_{\mathrm{equ}}} \frac{\partial \varepsilon_{\mathrm{equ}}}{\partial \underset{\sim}{\boldsymbol{\varepsilon}}} \tag{4.21}$$

$$\frac{\partial D_{\mathrm{v}}}{\partial D} = \frac{(\Delta t/\eta)}{1 + (\Delta t/\eta)} \tag{4.22}$$

$$\frac{\partial D}{\partial \kappa} = D' = \frac{\varepsilon_{\mathrm{f}}\varepsilon_{\mathrm{equ}}(\varepsilon_{\mathrm{f}} - \varepsilon_0) - \varepsilon_{\mathrm{f}}(\varepsilon_{\mathrm{equ}} - \varepsilon_0)(\varepsilon_{\mathrm{f}} - \varepsilon_0)}{(\varepsilon_{\mathrm{equ}}(\varepsilon_{\mathrm{f}} - \varepsilon_0))^2} = \frac{\varepsilon_{\mathrm{f}}\varepsilon_0}{\varepsilon_{\mathrm{equ}}^2(\varepsilon_{\mathrm{f}} - \varepsilon_0)} \tag{4.23}$$

$$\frac{\partial \kappa}{\partial \varepsilon_{\text{equ}}} = 1 \tag{4.24}$$

$$\frac{\partial \varepsilon_{\text{equ}}}{\partial \underset{\sim}{\varepsilon}} = \frac{(1/2)(1/E)\ 2\ \underset{\approx}{\mathbb{E}}^{0} : \underset{\sim}{\varepsilon}}{\sqrt{(1/E)\ \underset{\sim}{\varepsilon} : \underset{\approx}{\mathbb{E}}^{0} : \underset{\sim}{\varepsilon}}} = \frac{\underset{\approx}{\mathbb{E}}^{0} : \underset{\sim}{\varepsilon}}{E\sqrt{(1/E)\ \underset{\sim}{\varepsilon} : \underset{\approx}{\mathbb{E}}^{0} : \underset{\sim}{\varepsilon}}} = \frac{\underset{\approx}{\mathbb{E}}^{0} : \underset{\sim}{\varepsilon}}{E \cdot \varepsilon_{\text{equ}}} \tag{4.25}$$

It should be noted that equation 4.22 represents the derivative obtained when the explicit evolution scheme for the viscous damage variable shown in equation 4.17 is differentiated with respect to the inviscid damage variable. This ensures that the Abaqus time integration procedure, which uses an a priori unkown time step size Δt, is incorporated. Therefore the tangent stiffness tensor is calculated consistently from an algorithmic point of view. In equation 4.25 the square root corresponds to the energy norm equivalent strain, thus the derivative can be written in a shortened form [20].

The final form for the tangential stiffness tensor

$$\underset{\approx}{\mathbb{E}}^{\text{t}} = (1 - D_{\text{v}})\underset{\approx}{\mathbb{E}}^{0} - \frac{(\Delta t/\eta)}{1 + (\Delta t/\eta)} \frac{\varepsilon_{\text{f}}\varepsilon_{0}}{\varepsilon_{\text{equ}}^{2}(\varepsilon_{\text{f}} - \varepsilon_{0})} \frac{1}{E\varepsilon_{\text{equ}}} \frac{1}{(1 - D_{\text{v}})^{2}}\ \underset{\sim}{\boldsymbol{\sigma}} \otimes \underset{\sim}{\boldsymbol{\sigma}} \tag{4.26}$$

is obtained by inserting the derivatives (4.22) - (4.25) into equation (4.20) and by using the relation $\underset{\approx}{\mathbb{E}}^{0} : \underset{\sim}{\varepsilon} = (1 - D_{\text{v}})^{-1}\underset{\sim}{\boldsymbol{\sigma}}$ obtained from equation (4.3).

For the implementation in the UMAT-subroutine, it is necessary to transform this tangent stiffness tensor into a 6 × 6 matrix. This is quite simple for the first part of the tensor, since the stiffness matrix for isotropic materials $\underline{\underline{\boldsymbol{E}}}^{0}$ can be found in the literature. The transformation for the second part of the tensor on the other hand is based on the rules specified in appendix A.1.

The resulting tangent stiffness matrix then equals

$$\underline{\underline{\boldsymbol{E}}}^{\mathrm{t}} = (1-D_{\mathrm{v}}) \begin{bmatrix} \lambda+2\mu & \lambda & \lambda & 0 & 0 & 0 \\ \lambda & \lambda+2\mu & \lambda & 0 & 0 & 0 \\ \lambda & \lambda & \lambda+2\mu & 0 & 0 & 0 \\ 0 & 0 & 0 & \mu & 0 & 0 \\ 0 & 0 & 0 & 0 & \mu & 0 \\ 0 & 0 & 0 & 0 & 0 & \mu \end{bmatrix} - \frac{(\Delta t/\eta)}{1+(\Delta t/\eta)} \frac{D'}{E_0\ \varepsilon_{\mathrm{equ}}}$$

$$\cdot \frac{1}{(1-D_{\mathrm{v}})^2} \begin{bmatrix} \sigma_{11}\sigma_{11} & \sigma_{11}\sigma_{22} & \sigma_{11}\sigma_{33} & \sigma_{11}\sigma_{12} & \sigma_{11}\sigma_{13} & \sigma_{11}\sigma_{23} \\ \sigma_{22}\sigma_{11} & \sigma_{22}\sigma_{22} & \sigma_{22}\sigma_{33} & \sigma_{22}\sigma_{12} & \sigma_{22}\sigma_{13} & \sigma_{22}\sigma_{23} \\ \sigma_{33}\sigma_{11} & \sigma_{33}\sigma_{22} & \sigma_{33}\sigma_{33} & \sigma_{33}\sigma_{12} & \sigma_{33}\sigma_{13} & \sigma_{33}\sigma_{23} \\ \sigma_{12}\sigma_{11} & \sigma_{12}\sigma_{22} & \sigma_{12}\sigma_{33} & \sigma_{12}\sigma_{12} & \sigma_{12}\sigma_{13} & \sigma_{12}\sigma_{23} \\ \sigma_{13}\sigma_{11} & \sigma_{13}\sigma_{22} & \sigma_{13}\sigma_{33} & \sigma_{13}\sigma_{12} & \sigma_{13}\sigma_{13} & \sigma_{13}\sigma_{23} \\ \sigma_{23}\sigma_{11} & \sigma_{23}\sigma_{22} & \sigma_{23}\sigma_{33} & \sigma_{23}\sigma_{12} & \sigma_{23}\sigma_{13} & \sigma_{23}\sigma_{23} \end{bmatrix} \tag{4.27}$$

with λ, μ as the Lamé constants. Literature references for the derivation of the tangent stiffness tensor can be found in [21] and [20].

4.2.5. Calculation of the Elastic Energy and Dissipation

It is reasonable to calculate the specific elastic strain energy and the dissipation when the UMAT-subroutine is executed, because then these quantities are available for post-processing. Abaqus supplies the global strain energy and dissipation based on the values calculated at the integration points, which have to be stored in the corresponding variables supplied by the subroutine interface such as SSE, SPD, and SCD.

Two sources for energy dissipation have to be distinguished in the implemented damage model. The first cause of dissipation is damage formation and the second cause for dissipation originates from the viscous regularization. The elastic strain energy and these two dissipation densities are illustrated in Figure 4.2, which shows the viscous and inviscid stress response for the material parameter set and characteristic element length listed on top of the figure.

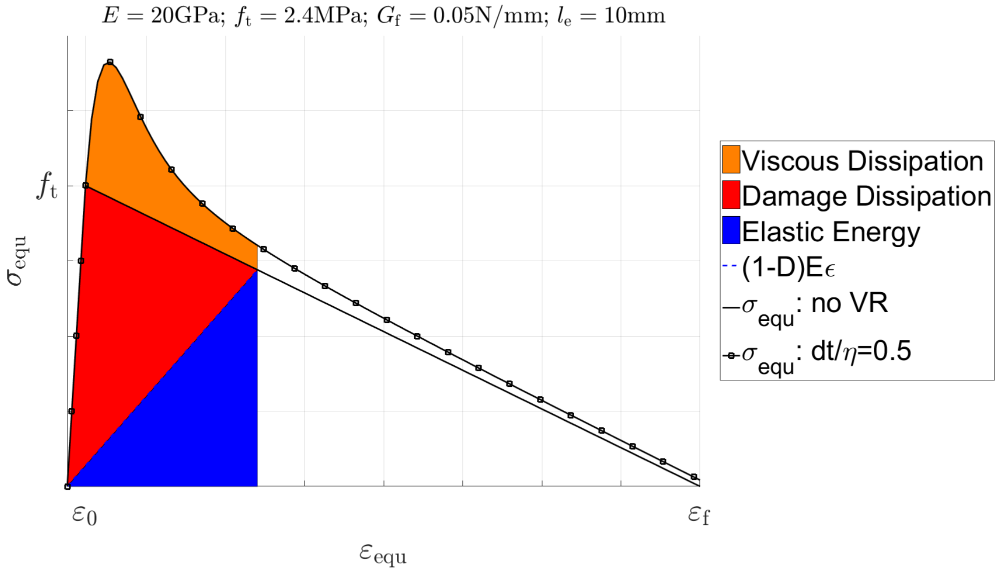

Figure 4.2.: Illustration of specific strain energy and dissipation caused by damage formation and viscous regularization. The linear softening represents the intended material behavior, while the line with square markers shows the viscous regularized material response. Graph obtained from a MATLAB simulation.

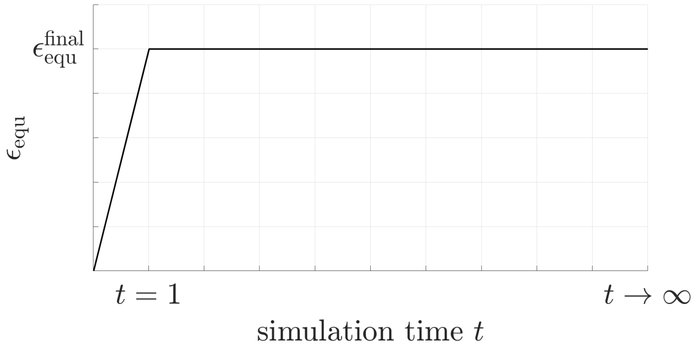

Figure 4.3.: Loading conditions for Figure 4.2, showing the time development of the applied strain.

The loading conditions shown in Figure 4.3, highlight that the viscous regularization has enough time in order for the stress to fully relax from the viscous curve to the inviscid curve. The following interpretation of Figure 4.2 is based on this assumption.

Each of the colored regions shown in Figure 4.2, correspond to a certain type of specific energy or specific dissipation. The triangular area below the damaged stiffness slope $(1-D)E_0$ corresponds to the elastically stored specific energy, which is written to the parameter *SSE*. The complementary triangle above the elastic energy represents the energy density dissipated due to damage formation. Its value is written to the parameter *SPD*, which is normally used to describe dissipation due to plastic deformation but is repurposed in this material model. Finally, the area above the linear softening behavior shows the dissipation density caused by viscous regularization. Its calculated value is written to the parameter *SCD*, which is intended to describe dissipation due to creep but is repurposed in this damage model implementation. This viscous dissipation area represents an unwanted deviation from the inviscid linear softening behavior, but is required to obtain converged numerical results. Nevertheless, the energy dissipation due to the implemented artificial viscosity should be kept as low as possible.

The energy and dissipation densities calculated during the UMAT execution are based on the following equations

$$e_{\mathrm{el}} = \mathrm{SSE} = \frac{1}{2}\,\underset{\sim}{\boldsymbol{\sigma}} : \underset{\sim}{\boldsymbol{\varepsilon}} = \frac{1}{2}(1-D)E\varepsilon_{\mathrm{equ}}^2 \tag{4.28a}$$

$$e_{\mathrm{D}} = \mathrm{SPD} = \text{area under inviscid linear curve} - \mathrm{SSE} = \frac{1}{2}\,DE\varepsilon_0\varepsilon_{\mathrm{equ}} \tag{4.28b}$$

$$e_{\mathrm{v}} = \mathrm{SCD} = \text{area under viscous curve} - \mathrm{SSE} - \mathrm{SPD} \tag{4.28c}$$

where e_{el}, e_{D} and e_{v} represent the specific elastic energy, dissipation density due to damage formation, and viscous regularization respectively. Equation (4.28a) shows that the scalar equivalent strain is used instead of the stress and strain tensors when the elastic energy density is calculated. This simplification is possible due to the energy norm definition for the equivalent strain according to equation 3.15. While the calculation of e_{el} and e_{D} is straightforward, it is not that simple to determine the dissipation density due to viscous regularization. This difficulty is caused by the fact that viscous regularization depends on the increment size Δt, which is chosen automatically by the numerical solver. Therefore it is required to sum up the incrementally applied specific work and subtract the specific strain energy and specific energy dissipation due to damage in order to calculate the specific viscous energy dissipation.

Again it is noted that the presented figure and equations are based on the assumption of a fully relaxed stress state, where the viscous damage variable converged towards the value of the inviscid damage variable ($D_{\mathrm{v}} \rightarrow D$). Since this is generally not the case during a simulation where the inviscid damage is still growing, the presented equations are merely an approximation. Nevertheless, the introduced error is negligible if the difference between viscous and inviscid damage variable is small.

5. Damage Simulations

In this chapter several example problems are presented, which are suited to test the performance and applicability of the developed elasto-damage constitutive law. Where available, the obtained numerical results are compared to references taken from published literature. The example problems include a single element verification, a uniaxial tensile test, two three-point bending tests, and a plate with circular hole under uniaxial tension.

5.1. Single Element - Damage Model Verification

Four aspects of the developed damage model are tested with this single element model. First of all, the linear strain-softening behavior is to be confirmed. Secondly the influence of viscous regularization on the stress-strain behavior is to be shown by comparing simulation results with different viscosity parameters. The third aspect tested is the elastic energy and energy dissipation output, which are compared to the externally applied work and the specified specific fracture energy. And finally the fourth aspect tested is the behavior upon load removal and reloading, where the damaged Young's modulus must remain constant during unloading and during the elastic part of the reloading step. A single linear hexahedral element (C3D8) with a size of 10mm×10mm×10mm, which is subjected to a uniaxial tensile test, is chosen as modeling approach. A displacement of $4.2 \times 10^{-2}\,\mathrm{mm}$ is applied to one surface, whereas it is set to zero on three surfaces as boundary condition as can be seen in Figure 5.1. This ensures that the Poisson contraction is unhindered. Table 5.1 lists the material parameters used for the numerical simulations, which are performed for a maximum increment size of $\Delta t_{\mathrm{max}} = 0.01\,\mathrm{s}$

Table 5.1.: Material parameters used for the damage model verification.

E	ν	ε_0	G_f
20 GPa	0.2	1.2e-04	50 J/m^2

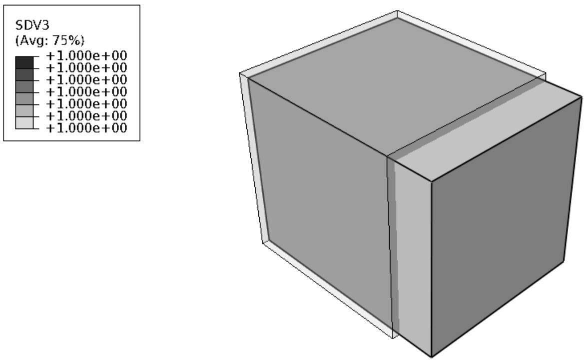

Figure 5.1.: Deformation and viscous damage variable SDV3 under uniaxial tension of the single element used for the damage model verification, with the initial shape as wire-frame and a deformation scaling factor of 50.

and a load step time of $t_\mathrm{end} = 1.0\,\mathrm{s}$, which results in a applied strain rate of $\dot{\varepsilon} = 0.0042\,\mathrm{s}^{-1}$. The three different artificial viscosity parameters used to demonstrate the influence of viscous regularization are $\eta = 1 \times 10^{-4}\,\mathrm{s}$, $\eta = 1 \times 10^{-3}\,\mathrm{s}$, and $\eta = 1 \times 10^{-2}\,\mathrm{s}$. Figure 5.2 shows the tensile stress and viscous damage variable results for three single element simulations. As can be seen, the numerical stress results exhibit linear strain softening behavior with the exception of the stress peak caused by the viscous regularization. Thus the implemented linear approach is verified. Furthermore, the figure shows that the deviation from the intended inviscid behavior increases if larger values for the artificial viscosity parameter η are used. While the deviation is negligible when the two smaller artificial viscosity parameters are used, it is quite pronounced for the simulation with $\eta = 1 \times 10^{-2}\,\mathrm{s}$, which exhibits a peak load height deviation of approximately 25%. This increased stress peak is caused by the slowed down growth of the viscous damage variable. As the stress-strain curves in Figure 5.2 highlight, the deviation from the

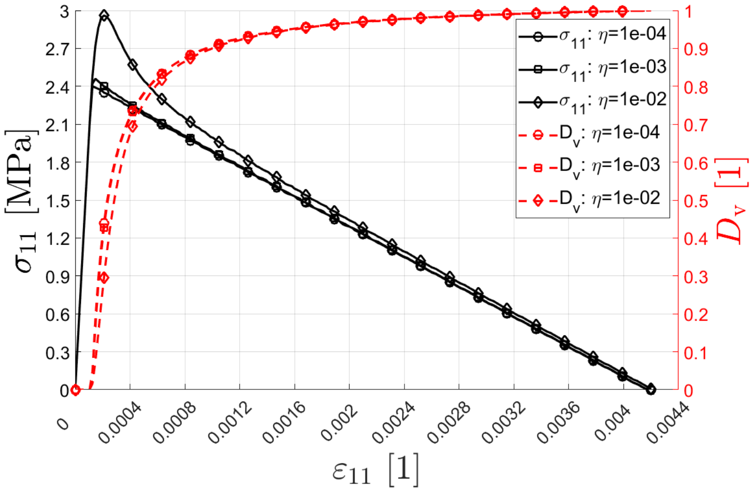

Figure 5.2.: Numerical results for the three single element damage model verification simulations showing a stress-strain diagram including the viscous damage variable D_{v} obtained for a uniaxial tensile test.

intended inviscid behavior is negligible if the artificial viscosity parameter is at least three orders of magnitude smaller than the simulation step time t_{end}.

The development of elastic strain energy and energy dissipation is plotted in Figure 5.3. It can be seen that the dissipation due to damage formation ALLPD is independent of the chosen artificial viscosity parameter, because it is determined by the inviscid damage variable D. ALLCD on the other hand clearly depends on the implemented viscosity, since it represents the amount of energy linked to the stress-magnification and thus the dissipation caused by viscous regularization. In order to keep the influence on the numerical results low, it is important that the energy dissipated due to viscous regularization remains small compared to the energy dissipated by damage formation. As can be seen, the elastic strain energy ALLSE does only change to a small degree when the artificial viscosity is varied. This can be attributed to the fact that the stress-magnification caused by viscous regularization is declining for increasing strain values, which keeps the deviation of ALLSE in check. Dividing the final value of ALLPD with the cubes cross section yields

$$5\,\mathrm{mJ}/100\,\mathrm{mm}^2 = 0.05\,\mathrm{mJ}/\mathrm{mm}^2 = 50\,\mathrm{J}/\mathrm{m}^2 \tag{5.1}$$

which is equal to specified specific fracture energy parameter G_f. Therefore the dissipation due to damage formation is verified.

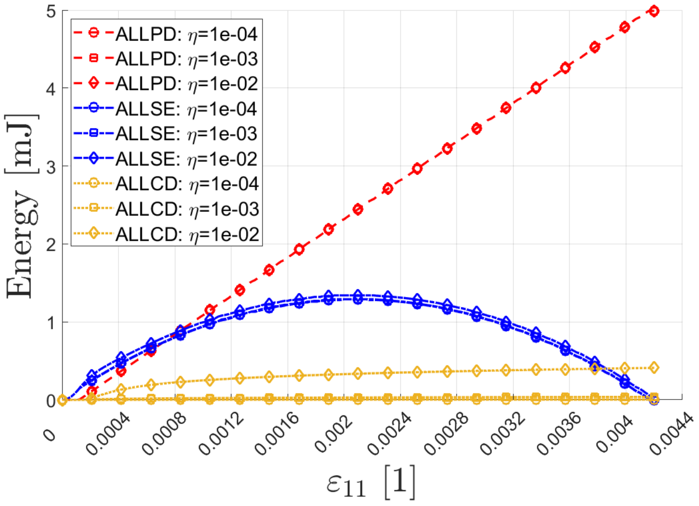

Figure 5.3.: Numerical results for the three single element damage model verification simulations showing ALLSE (elastic energy), ALLPD (dissipation due to damage formation), and ALLCD (dissipation due to viscous regularization) for a uniaxial tensile test.

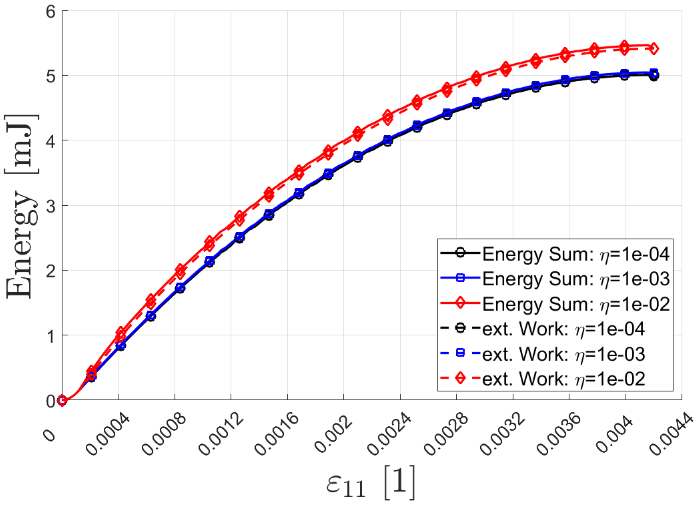

Figure 5.4.: Numerical results for the three single element damage model verification simulations showing the energy sum (ALLSE+ALLPD+ALLCD) and the externally applied work for a uniaxial tensile test.

Finally Figure 5.4 is given, which verifies that the sum of strain energy ALLSE, energy dissipation due to damage formation ALLPD, and energy dissipation due to viscous regularization ALLCD is equal to the externally applied work. This highlights that the stress, elastic energy and dissipation results correspond to each other. However, it should be noted that the chosen calculation approach for the energy dissipation due to damage formation does lead to a small deviation between the externally applied work and the sum of ALLSE, ALLPD, and ALLCD. This deviation increases when the effect of viscous regularization is more pronounced and is caused by fact that energy dissipation due to damage formation is implemented to depend on the inviscid damage variable D, which corresponds to the case of a fully relaxed stress state where $D_\mathrm{v} \to D$.

Finally the behavior upon load removal and subsequent reloading is shown in Figure 5.5, where the stress and viscous damage variable are shown for three simulation steps performed with an artificial viscosity of $\eta = 1 \times 10^{-4}\,\mathrm{s}$ and a simulation step time of $t_\mathrm{end} = 1.0\,\mathrm{s}$. In the first simulation step a displacement of $1.0 \times 10^{-2}\,\mathrm{mm}$ is applied, which is removed in the second step, whereupon a reloading step is applied with a displacement of $4.2 \times 10^{-2}\,\mathrm{mm}$. The figure confirms that the damaged Young's modulus remains constant upon load removal.

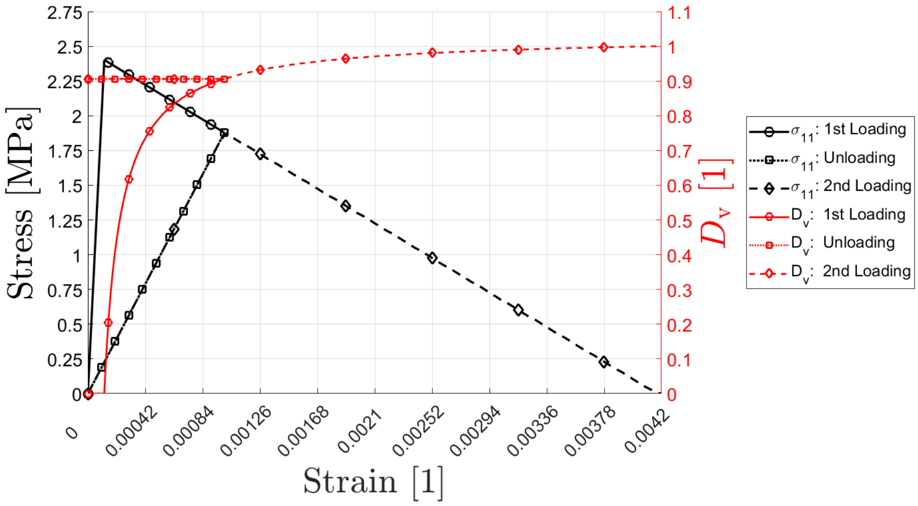

Figure 5.5.: Numerical results for the damage model verification, showing the behavior upon load removal and reloading.

5.2. Bar Under Uniaxial Tension

In this section, it is demonstrated that the developed constitutive law can produce results that are independent of the chosen mesh-size. However, it is important to remember that objective results are only obtained if damage localizes into a single layer of elements as described in sections 3.5.2 and 4.2.2. Since the model would exhibit uniform damage distribution when no counter-measures are taken, it is required to induce localization. This is done by applying an initial damage of $D_0 = D_{\mathrm{v}0} = 0.1$ to a row of elements. It should be noted that the amount of energy dissipation linked to this initial damage is approximately two orders of magnitude lower than the total amount of dissipated energy. Therefore the results are not compromised by this approach. Nevertheless, the fact that special measures are required in order to obtain objective results highlights the downside of the implemented mesh-adjusted softening regularization.

The chosen modeling approach is a bar with quadratic cross section (45mm × 45mm × 225mm), which is discretized with linear hexahedral elements (C3D8). Three simulation models with different element sizes are used (45mm, 15mm, and 5mm), which are named in the following as coarse, medium, and fine mesh. The displacement in axial direction set to zero on the left side of the bar as boundary condition. A poisson ratio of zero is chosen to avoid any effects resulting from contraction. A displacement of 0.1mm is applied on the right side of the bar, which is sufficient to cause total rupture. Table 5.2 lists the material parameters used in the simulations, which are performed with an artificial viscosity parameter of $\eta = 1 \times 10^{-4}\,\mathrm{s}$ and a simulation step time of $t_{\mathrm{end}} = 1.0\,\mathrm{s}$. The viscous damage variable field and displacement field results shown in Figure 5.6 confirm the localization into a single layer of elements. Furthermore, the displacement field shows that the macroscopic crack is represented as “displacement jump”, which fits the geometric interpretation of cracks.

Table 5.2.: Material parameters used for the bar under uniaxial tension.

E	ν	ε_0	G_f
20 GPa	0.0	1e-04	90 J/m^2

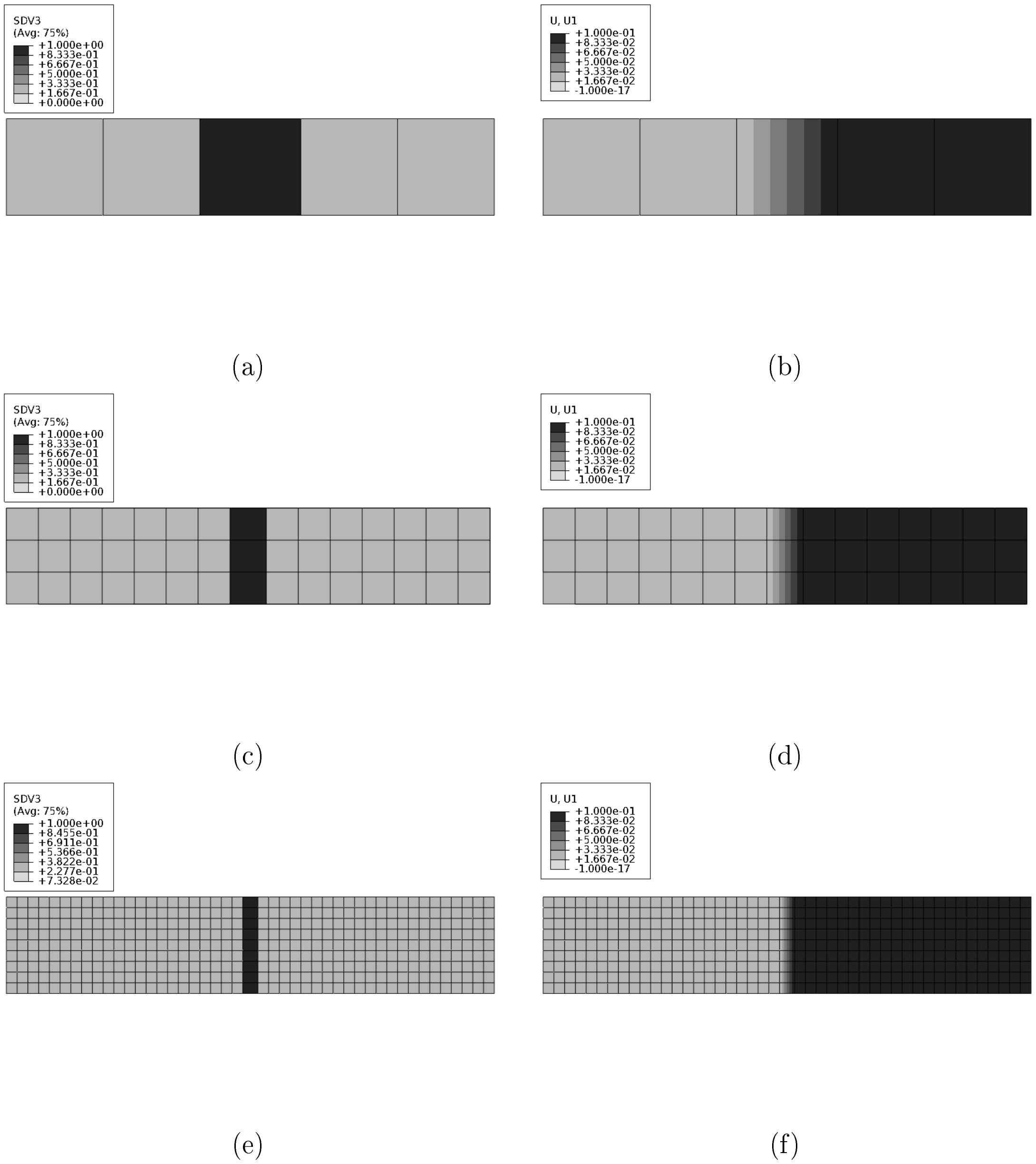

Figure 5.6.: Simulation results for the bar under uniaxial tension showing the viscous damage variable SDV3 (a)(c)(e) and displacement field U1 (b)(d)(f) for the coarse, medium, and fine mesh respectively.

Finally, the global results of the entire bar for all three meshes are given in Figure 5.7, which shows the obtained load-displacement curve, elastic strain energy ALLSE, and energy dissipation due to damage ALLPD. As can be seen, the numerical results only show a negligible mesh size dependence, which verifies that the developed damage model yields objective results if damage localizes into a single layer of elements. It should be noted that the small deviation for the fine mesh results are attributed to the fact that damage formation occurred to a small degree in the entire specimen before localization set in.

To verify the energy dissipation results due to damage formation, the value at final rupture is divided by the bar's cross-section

$$\approx 182\,\mathrm{mJ}/(45\,\mathrm{mm})^2 = 0.089\,87\,\mathrm{mJ/mm^2} = 89.87\,\mathrm{J/m^2} \tag{5.2}$$

which is in good agreement with the specified specific fracture energy G_f, thus the dissipation results are verified. Finally it should be mentioned that the amount of dissipation due to viscous regularization ALLCD is negligible with values in the order of $1 \times 10^{-1}\,\mathrm{mJ}$.

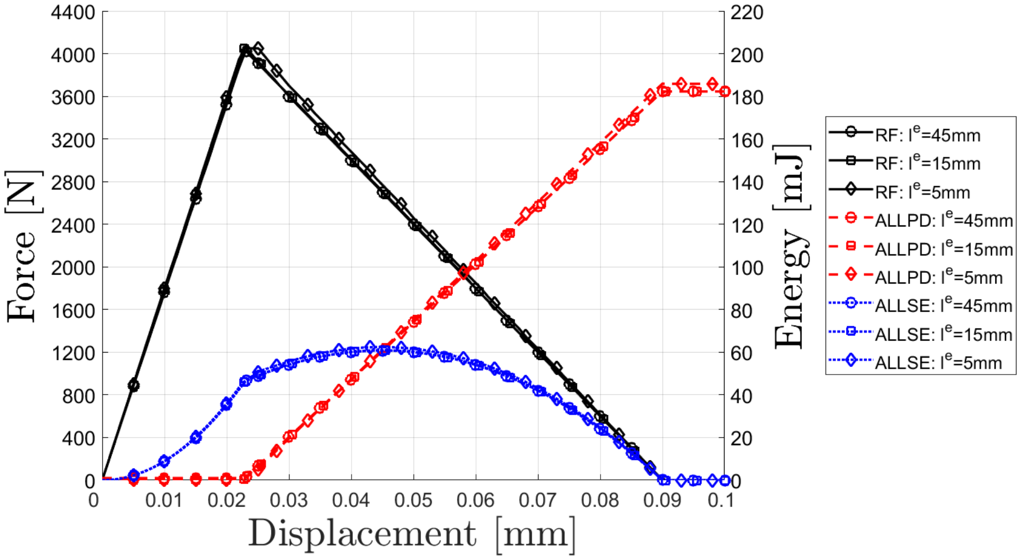

Figure 5.7.: Numerical results for the bar under uniaxial tension showing the global reaction force, the elastic energy (ALLSE) and dissipation due to damage (ALLPD) as a function of the applied displacement.

5.3. Three-Point Bending Test 1

A three-point bending test of a notched beam meshed with plane-strain elements is chosen to demonstrate that the developed damage model is able to give reasonable predictions. This is achieved by comparing the obtained numerical results to a literature reference shown in Figure 5.8.

As can be seen, the reference mesh is refined at the beam's center but is more coarse at the outer thirds in order to reduce the simulation time. While the center elements are equal to the notch width with an element size of 5 mm, the larger elements in the coarse part have a size of 20 mm. The boundary conditions used in the literature reference are shown in Figure 5.8 (a), and a displacement load of 0.5 mm is applied at both top nodes of the top element on the notch path. Table 5.3 lists the used material parameters.

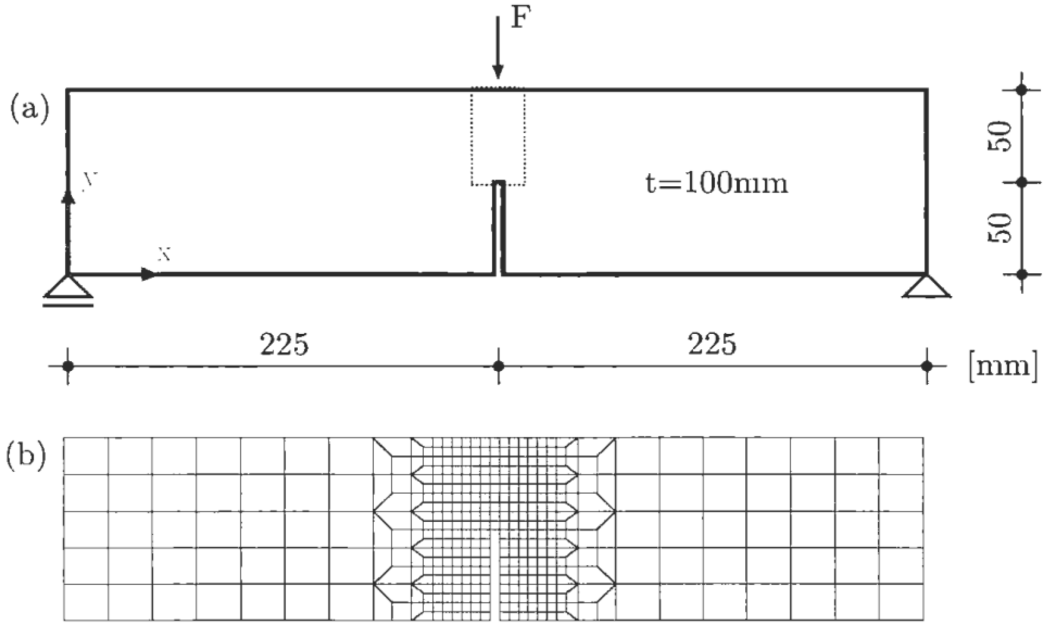

Figure 5.8.: Literature reference [20] of a notched beam subjected to a three-point bending test with 5 mm notch width, showing the geometry, mesh, boundary conditions.

Table 5.3.: Material parameters used for the three-point bending test 1 [20].

E	ν	ε_0	G_f
20 GPa	0.2	1.2e-04	90 J/m^2

In order to test the developed damage model, the displayed three-point bending test is simulated for three different settings. Each simulation uses linear plane-strain elements (CPE4) and is performed for the geometry, boundary conditions, and applied load specified in the reference. The first simulation repeats the described reference situation from [20] exactly. The second and third simulations, however, use a refined mesh where the center part of the beam is meshed with elements half the reference size. Since damage did not localize in a single layer of elements in the second simulation, localization is induced in the third simulation by applying a 10% higher tensile strength to all elements except those on the macroscopic crack path. All simulations use an artificial viscosity parameter of $\eta = 1 \times 10^{-4}\,\mathrm{s}$ and a simulation step time of $t_\mathrm{end} = 1.0\,\mathrm{s}$. The deformed specimen and the viscous damage variable distribution for the three simulation settings are shown in Figure 5.12.

For a better comparability Figure 5.9 is given, which shows the obtained numerical results for the reference mesh with the literature reference as background image. Figures 5.10 and 5.11 show the separate load-displacement curves for the literature reference and the performed simulations, respectively. A comparison highlights that the developed elasto-damage model yields reasonable results, since the obtained load-displacement diagram is nearly identical to the reference. since the obtained load-displacement diagram is nearly identical to the reference. Nevertheless there are certain differences, such as a different shape of the curve in the post-peak region. This different post-peak shape can be attributed to the implemented type of strain-softening behavior, which is linear for the developed model and exponential for the reference. In addition to this shape difference, the literature reference peak load is higher and occurs at a larger displacement value. A possible cause for this peak load height difference is the different equivalent strain definition. While the reference is using a standard rankine description, the implemented model uses the energy norm.

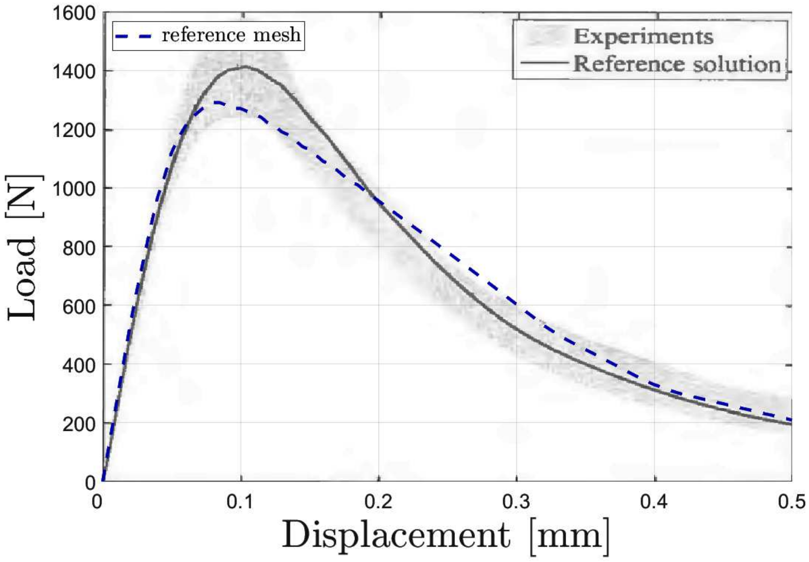

Figure 5.9.: Combined load-displacement diagram showing the obtained reference mesh results with the literature reference as background image.

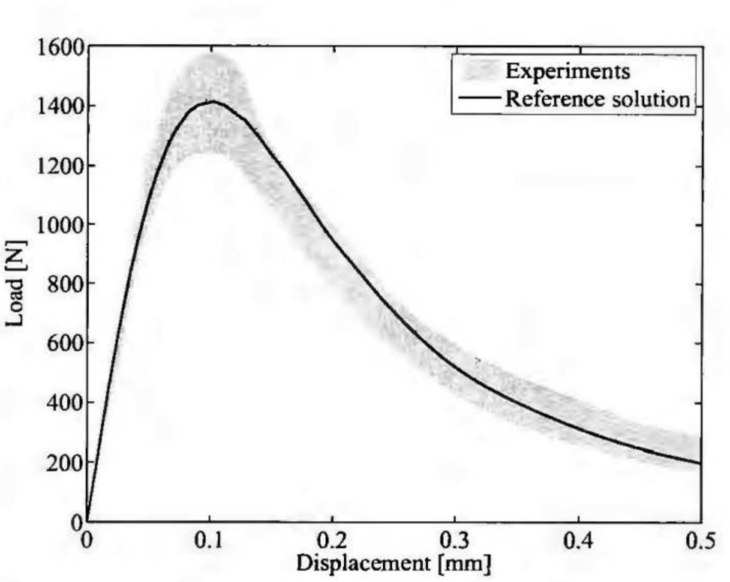

Figure 5.10.: Literature reference [20] load-displacement results of the three-point bending test 1.

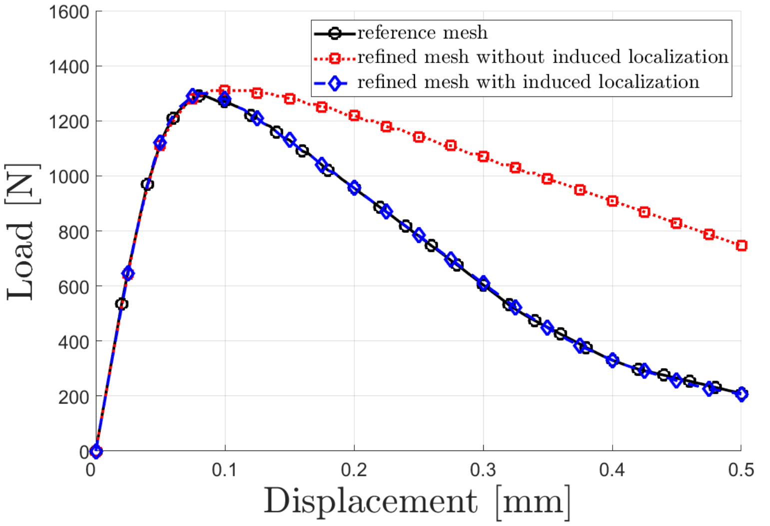

Figure 5.11.: Abaqus simulation results of the three-point bending test 1 in form of a load-displacement curve, showing the results for the reference mesh, refined mesh without induced localization, and refined mesh with induced localization.

Figure 5.11 shows the obtained load-displacement results for the three simulation settings, reference mesh, refined mesh without induced localization, and refined mesh with induced localization. As can be seen, the reference mesh results are identical to the results obtained on the refined mesh with induced localization. The results on the refined mesh without induced localization on the other hand, deviate dramatically from the other two curves. This demonstrates the capability and limitation of the implemented mesh-adjusted softening regularization, which ensures objective results only if damage localizes into a single layer of elements. The cause for this behavior is the requirement that the localization width must be equal to the length parameter used in the regularization. This length parameter, however, is based on the characteristic element length, thus the single element layer localization requirement. In cases where damage is not confined in a single element layer, it is required to induce localization in order to obtain objective results.

Finally it should be noted that the amount of energy dissipated due to viscous regularization is in the order of 1×10^{-1} mJ and therefore negligible.

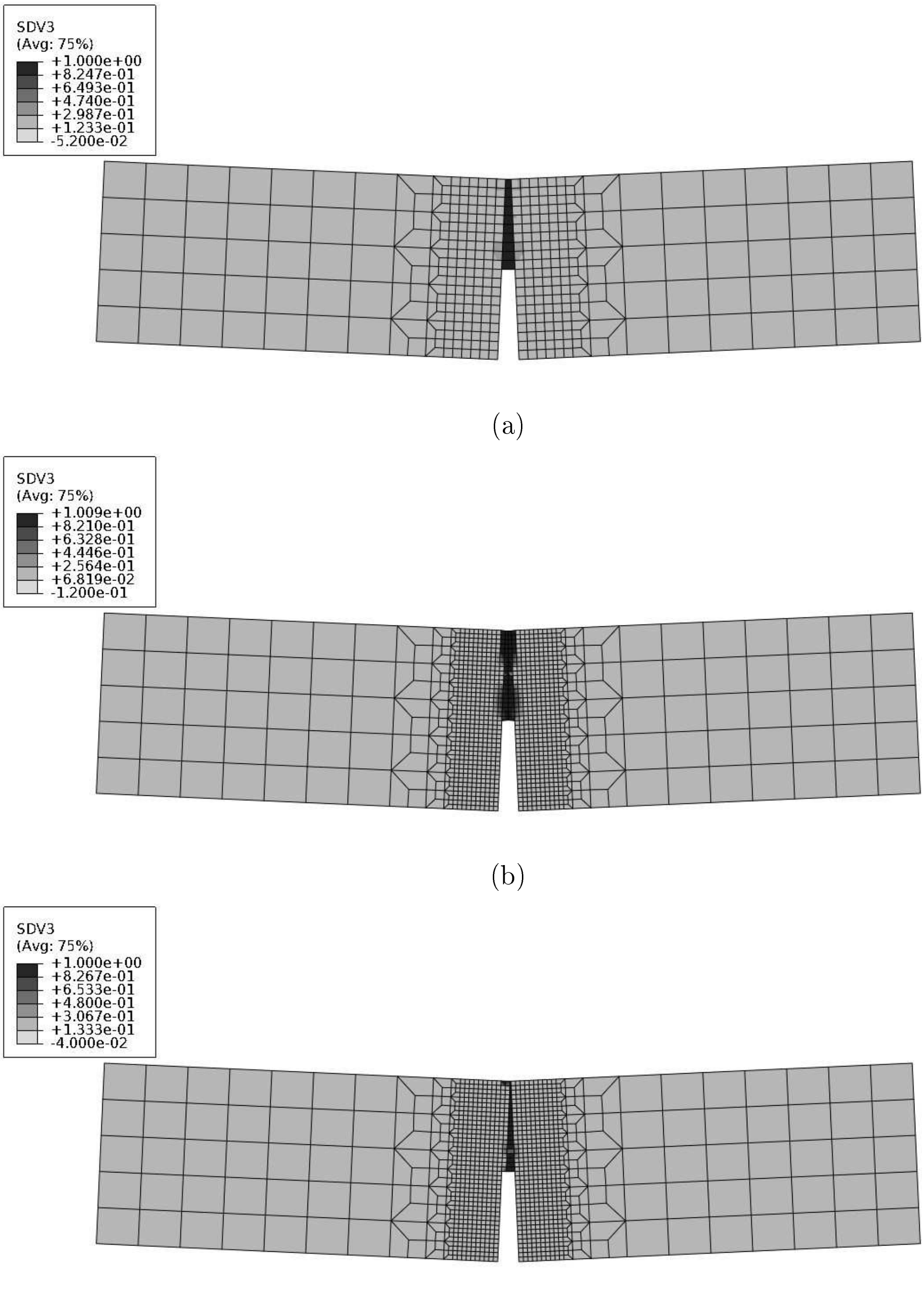

(a)

(b)

(c)

Figure 5.12.: Deformed shape and viscous damage variable SDV3 distribution for the three-point bending test 1, with (a) reference mesh, (b) refined mesh without induced localization, and (c) refined mesh with induced localization.

5.4. Three-Point Bending Test 2

A second literature reference example [21] for a three-point bending test is presented here, which is used as comparison for the results obtained with the developed damage model. The modeling approach shown in Figure 5.13 consists of three beams with different notch lengths, which are modeled with linear plane-strain elements (CPE4). The elements on the crack path have an aspect ratio of one and a size of 5 mm, whereas the elements on the left and right part are elongated with a length of approximately 20 mm. The boundary conditions are chosen according to the presented figure, with the left corner node completely fixed and the right corner node fixed only in vertical direction. The simulations are performed with an applied displacement of 1.5 mm on both top nodes of the top element on the crack path. The used material parameters are listed in Table 5.4. The simulations

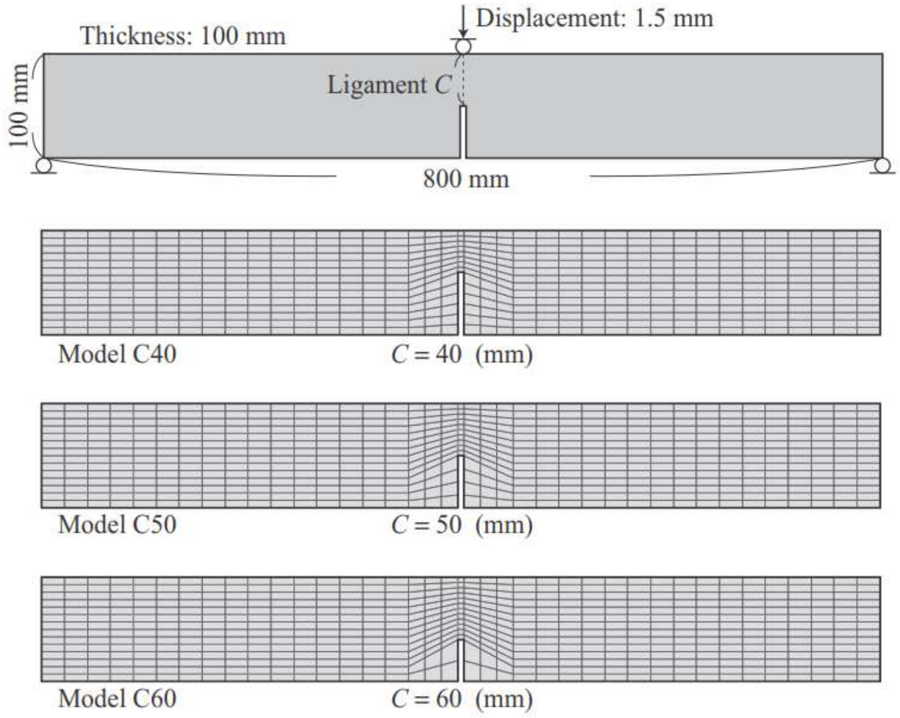

Figure 5.13.: Literature reference [21] for a three-point bending test, showing the geometries, meshes, load, and boundary conditions of three notched beams, where C represents the remaining ligament length.

Table 5.4.: Material parameters used for the three-point bending test 2 [21].

E	ν	ε_0	G_f
30 GPa	0.0	1e-04	$100\,\mathrm{J/m^2}$

are performed with an artificial viscosity parameter of $\eta = 1 \times 10^{-4}\,\mathrm{s}$ and a step time of 1.0 s. For a better comparability, the obtained load-displacement diagram is shown with the literature reference as background image in Figure 5.14. Figures 5.15 and 5.16 show these load displacement diagrams separately. A comparison highlights that both exhibit similar behavior, they feature approximately the same peak load change from beam to beam, and they converge into a common curve. The results, however, also exhibit certain differences. First of all the exponential strain-softening description compared to the implemented linear approach is clearly visible. Secondly, the literature reference peak load value for each beam is higher

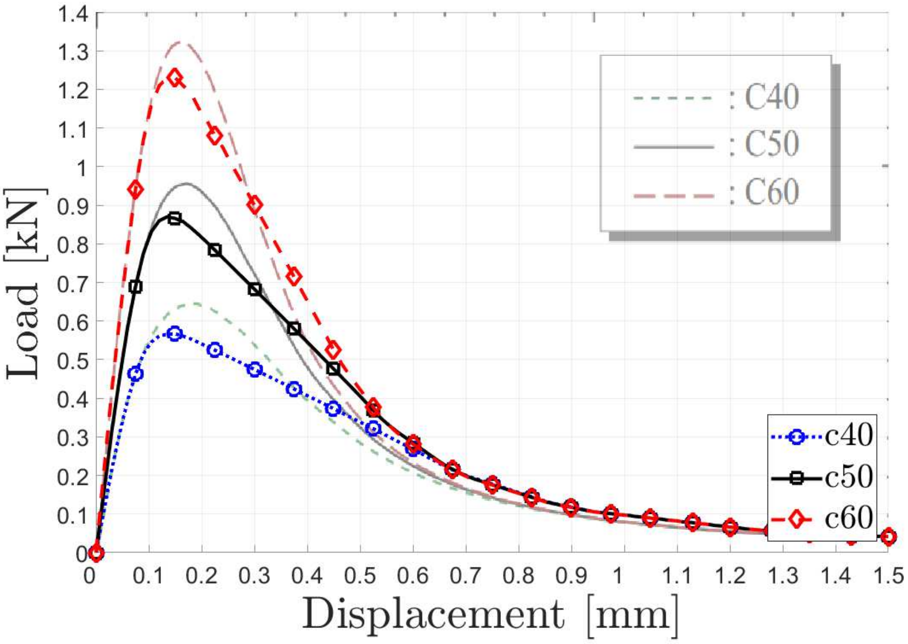

Figure 5.14.: Combined load-displacement diagram showing the obtained numerical results for the three-point bending test 2 with the literature reference as background image.

and occurs at a larger displacement value. A possible cause for this difference in the peak load height is the different equivalent strain definitions used. While the implemented damage model uses the energy norm, the literature reference uses a modified von-Mises definition that does not take into account the energy share caused by volume change.

The deformed specimen and distribution of the viscous damage variable SDV3 are shown in Figure 5.17. As can be seen, the simulation meshes are equal to those used in the literature reference. The reason why three beams with different notch lengths are used is that Kurumatani et al. [21] suggest a method to determine the specific fracture energy. According to this approach, the specific fracture energy is obtained when the difference in the applied mechanical work between two beams is divided by the difference in the fracture surface areas, which is caused by the different notch lengths. Applied to the obtained numerical results one gets

$$G_{\mathrm{f}}^{50-40} = 100.05\,\mathrm{J/m^2} \tag{5.3}$$

by comparing beams C50 and C40, and

$$G_{\mathrm{f}}^{60-50} = 100.14\,\mathrm{J/m^2} \tag{5.4}$$

when beams C60 and C50 are compared. Both results match the specified specific fracture energy value quite well, which verifies the results obtained with the developed damage model. The basic assumption for this method is that the difference in mechanical work, which can be obtained by subtracting the areas enclosed in the force-displacement diagram, is consumed in the formation of crack area corresponding to the different notch lengths.

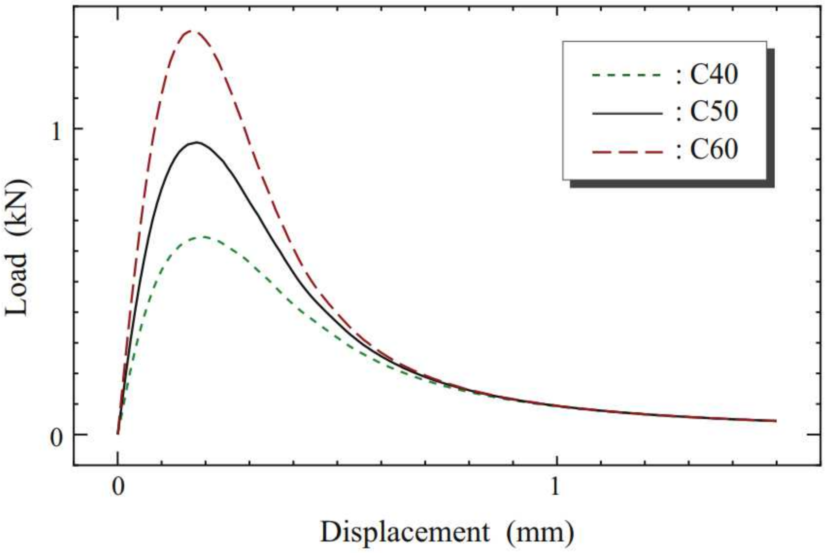

Figure 5.15.: Literature reference results of the three-point bending test 2 in form of a load-displacement curve [21].

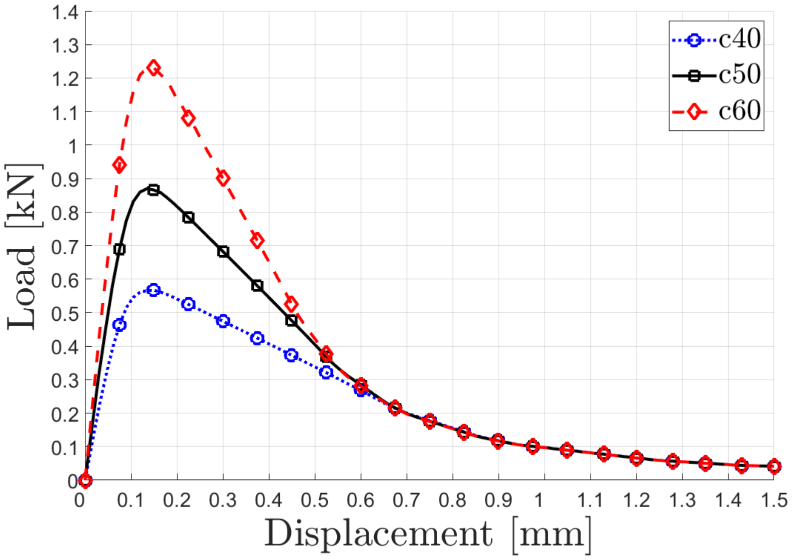

Figure 5.16.: Simulation results for the three-point bending test 2, showing the load-displacement results of the three notched beams with different notch lengths.

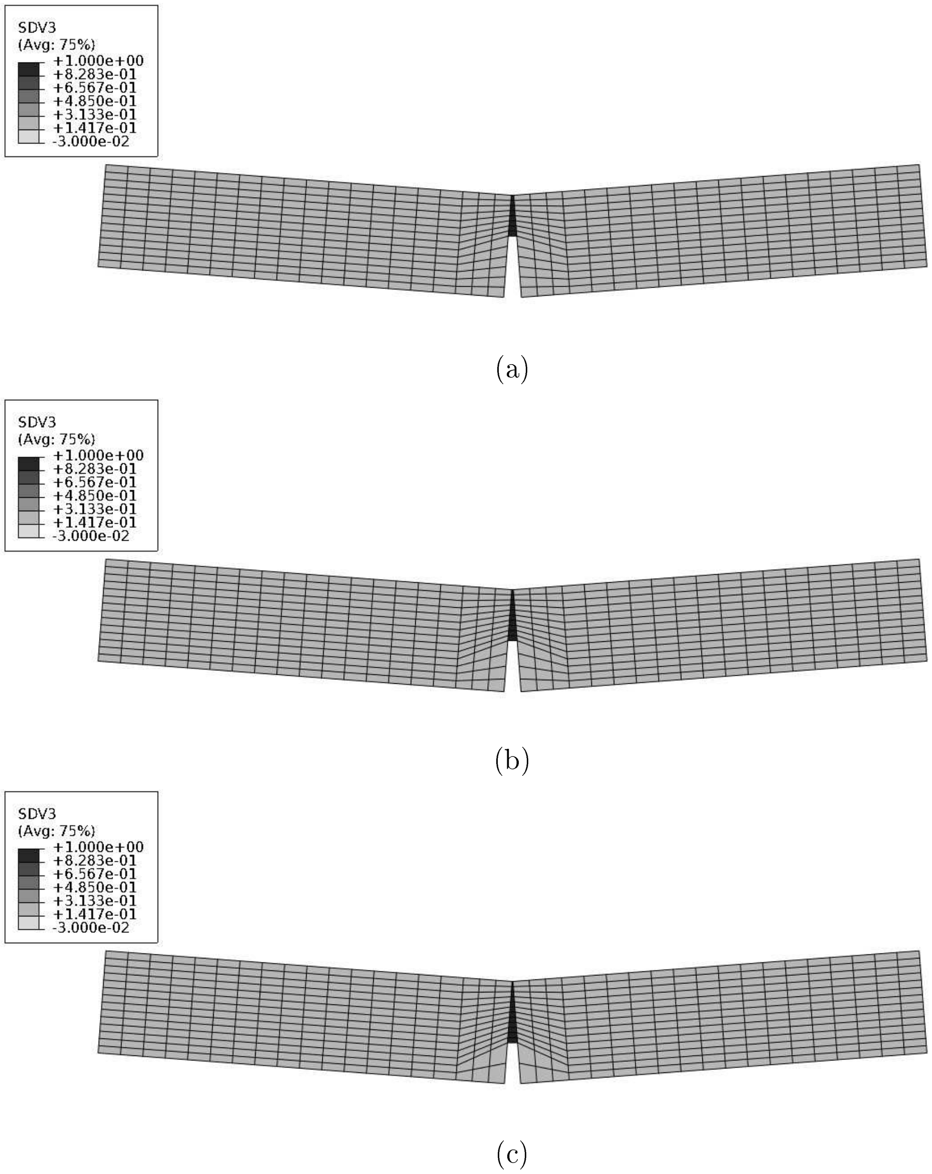

(a)

(b)

(c)

Figure 5.17.: Deformed shape and viscous damage variable SDV3 distribution of the notched beams in the three-point bending test 2 with (a) model C40, (b) model C50, and (c) model C60.

5.5. Plate with hole under uniaxial tension

The presented example problem is taken from a paper by Kurumatani et al. [21] and displayed in Figure 5.18, where three simulation models (H1, H2 and H3) are shown for a plate with circular hole under uniaxial tension. These literature reference simulation models are modeled with linear plane strain triangular elements. The plates are constrained at the bottom edge and get a displacement applied on the top. Model H1 represents a scaled down version of the model H2, where both the dimensions and applied displacement is halved but the number of elements is kept the same. Model H3 on the other hand has the same dimensions and applied displacement as model H2 but uses the element size from model H1, thus it is twice as fine meshed.

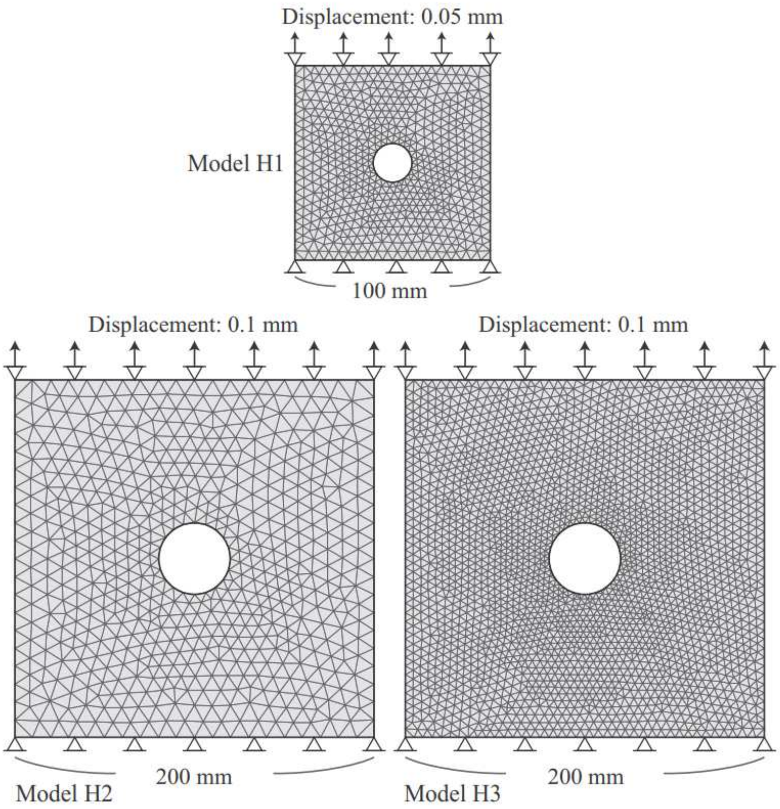

Figure 5.18.: Literature reference [21] of plates with a circular hole subjected to a tensile test, showing the geometries with 20 mm and 40 mm hole diameter, and showing the meshes, boundary conditions, and loads.

Table 5.5.: Material parameters for the plate with hole example problem [21].

E	ν	ε_0	G_f
20 GPa	0.1	1e-04	40 J/m^2

In the literature reference, the presented simulation approach is used to show that mesh size independent results can be obtained with their elasto-damage model, which is done by comparing the results for models H2 and H3. Furthermore, the size-effect, a characteristic behavior for brittle materials with strain-softening fracture, can be demonstrated. This dependence on the model size is shown by comparing the results for model H1, with half the size, to the results for the models H2 and H3. The literature reference simulations use the geometries, meshes, boundary conditions, and load specified in Figure 5.18 and the material parameters listed in Table 5.5.

These reference simulations are repeated with the damage model developed within the scope of this thesis, once for a linear plane-strain triangular element (CPE3) mesh corresponding to the reference and once for a linear quadrilateral element (CPE4) mesh. The simulations are performed with an artificial viscosity parameter $\eta = 1 \times 10^{-4}$ s and a step time of 1.0 s. It should be noted that the tria-element simulations use a correction factor of CF $= 1.4$, that compensates the difference between characteristic element length and actual width of failed elements, as described in Section 4.2.2. The boundary conditions are applied in accordance to the reference, where the vertical displacement for the bottom nodes is set to zero. In addition, the horizontal displacement for the corner nodes is prevented as well. The displacement load used in the reference, where 0.05 mm are applied on the H1 model and 0.10 mm on the H2 and H3 models, is also used in the performed simulations. The resulting viscous damage variable SDV3 distribution is shown in Figure 5.19, where it can be seen that the crack path is straight for the quadrilateral element mesh and curved for the triangular element mesh. Interestingly the crack path shape seems similar for all three tria-element models, as can be seen by comparing figures (b), (d) and (f). Furthermore, damage appears to be spread over several elements in the tria-mesh simulations, whereas it is constrained in a single element layer in the quad-mesh.

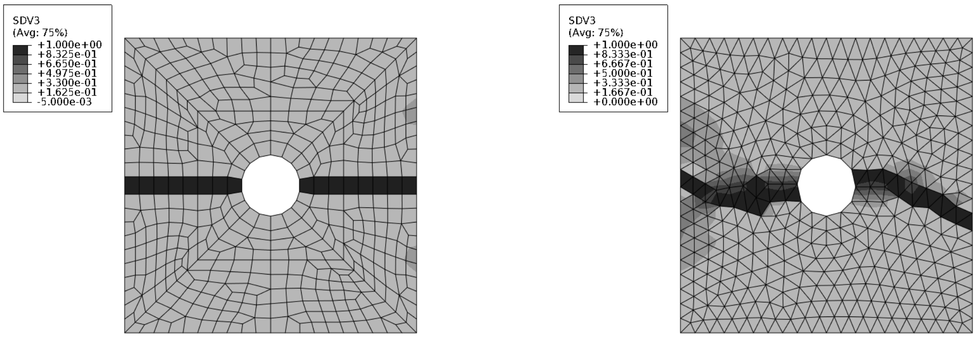

(a) SDV3 for Model H1 (b) SDV3 for Model H1

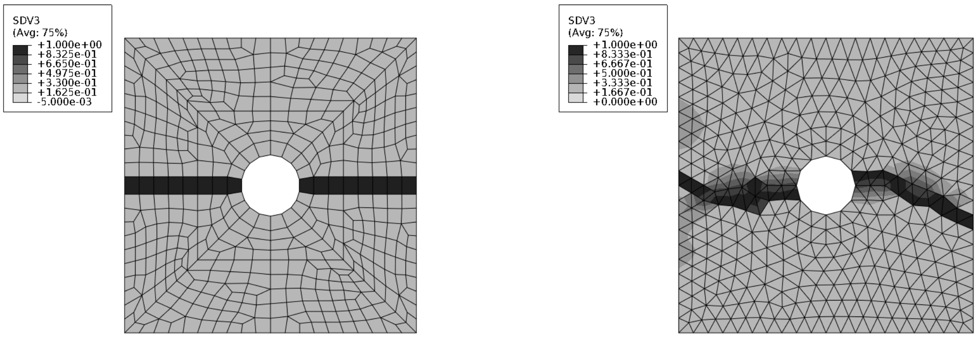

(c) SDV3 for Model H2 (d) SDV3 for Model H2

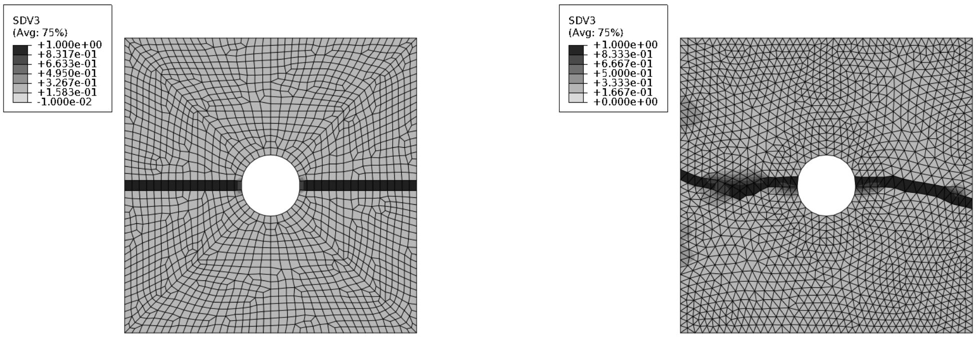

(e) SDV3 for Model H3 (f) SDV3 for Model H3

Figure 5.19.: Viscous damage variable SDV3 distribution for the plate with circular hole under tensile load, with (a), (c) and (e) showing the quad-element models and (b), (d) and (f) the tria-element models.

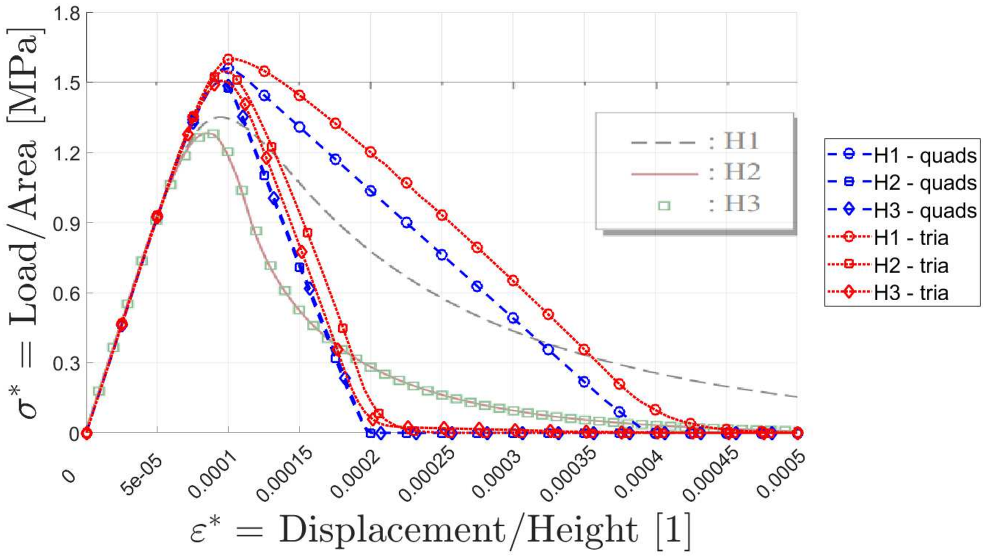

Figure 5.20.: Combined apparent stress-strain diagram showing the obtained numerical results for the plate with circular hole example problem with the literature reference as background image.

For a better comparability, Figure 5.20 is given, which shows the obtained results with the literature reference as background image. Figures 5.21 and 5.22 show the apparent stress-strain results for the literature reference and the performed simulations, respectively. These apparent stress-strain diagrams plot the applied force divided by the plate's cross-section against the applied displacement divided by the plate's height, which allows the comparison of plates with a different size. Comparing the obtained numerical results to the literature reference highlights that the obtained results exhibit linear strain-softening behavior compared to the exponential softening in the reference. Furthermore, the peak load of the obtained numerical results is significantly higher than in the reference case. The different equivalent strain definitions used in the implemented model compared to the reference poses a possible cause for this difference in peak load height. While the implemented model uses the energy norm definition, the reference relies on a modified von-Mises definition with a compressive strength ten times as high as the tensile strength. The displayed difference is quite prominent and might indicate that an exponential strain-softening and a linear strain-softening description are just too different in order to obtain similar results.

Aside from the obvious difference between reference and obtained results, there are certain similarities as well. Both of the element types used in the simulations are able to reproduce the size-effect shown in the reference results, where the smaller H1 model exhibits more pronounced dissipation compared to the larger H2 and H3 models. This size-effect is typical for materials with strain-softening behavior and the fact that it is reproduced in a numerical simulation highlights the suitability of the developed damage model. Furthermore, the results obtained for the H2 and H3 models, where the plates have equal size but are meshed with a different resolution, are fairly equal. This is especially true in the case of the quadrilateral mesh simulations, whereas there is still a slight mesh size dependence in the triangular mesh results. These fairly equal results obtained on differently fine meshed simulation models demonstrate that relatively objective results are obtained. Finally, the curved crack path compared to the straight line crack shown in Figure 5.19 is given as possible cause for the clearly visible difference in the obtained results for the quadrilateral and triangular mesh simulations.

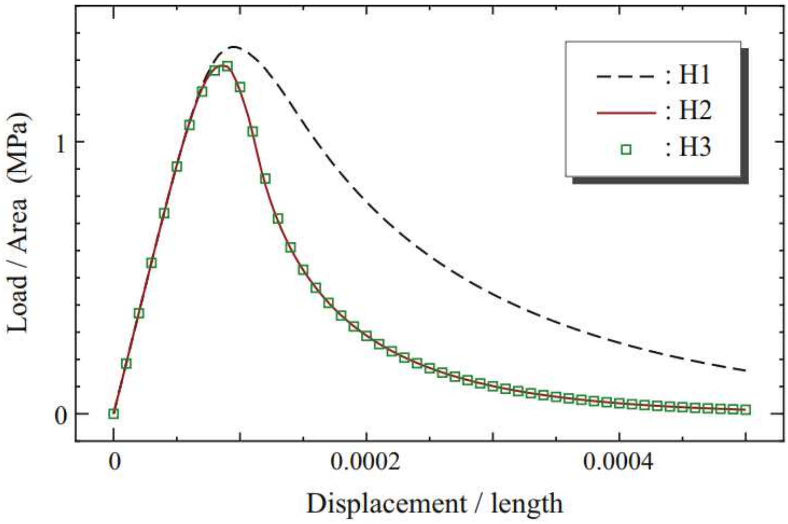

Figure 5.21.: Literature reference results for the plate with circular hole example problem as an apparent stress-strain diagram [21].

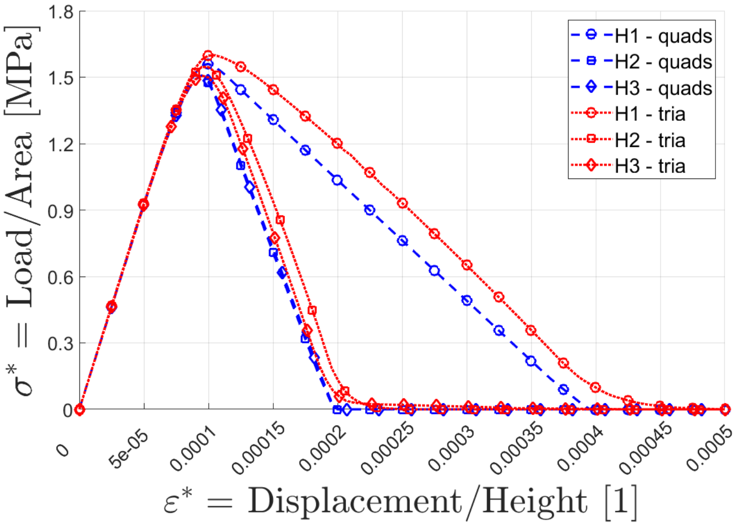

Figure 5.22.: Numerical results for the plate with circular hole under uniaxial tension showing an apparent stress-strain diagram for the H1, H2, and H3 models, with the quadrilateral mesh results shown as blue dashed line and the triangular mesh results shown as red dotted line.

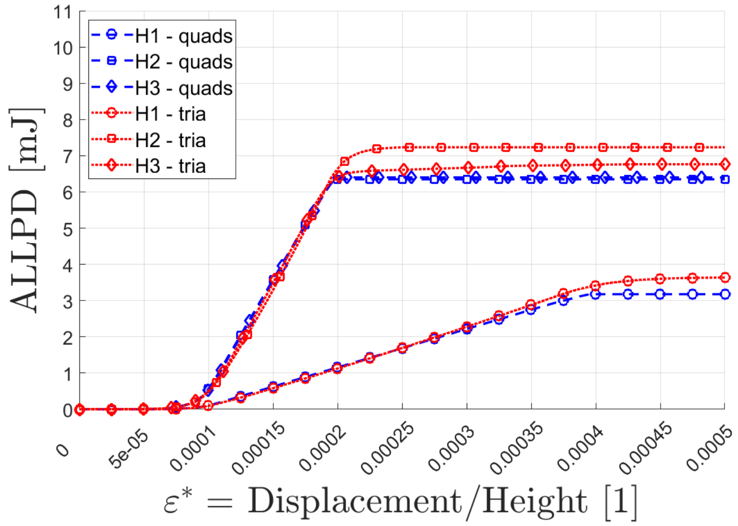

Figure 5.23.: Numerical results for the plate with circular hole under uniaxial tension showing the energy dissipated due to damage formation ALLPD for a plate thickness of 1 mm, where the quadrilateral mesh results are shown as blue dashed line and the triangular mesh results are shown as red dotted line.

Figure 5.23 shows the energy dissipation due to damage formation ALLPD for a plate thickness of 1 mm. By comparing the quadrilateral element results for the H2 and H3 models, it can be seen that mesh size independent results are obtained. The same comparison for the triangular element results on the other hand shows that these simulations still exhibit a slight mesh size sensitivity. This observation is in agreement to the conclusion drawn from the apparent stress-strain diagram.

To check the plausibility of the obtained dissipation results, the energy dissipated at final rupture is divided by the plate's cross-section at the crack path. This yields

$$\approx 3.2\,\mathrm{mJ}/(80\,\mathrm{mm}\cdot 1\,\mathrm{mm}) = 0.04\,\mathrm{mJ}/\mathrm{mm}^2 = 40\,\mathrm{J}/\mathrm{m}^2 \tag{5.5}$$

for the H1 model simulated with quadrilateral elements, and

$$\approx 6.4\,\mathrm{mJ}/(160\,\mathrm{mm}\cdot 1\,\mathrm{mm}) = 0.04\,\mathrm{mJ}/\mathrm{mm}^2 = 40\,\mathrm{J}/\mathrm{m}^2 \tag{5.6}$$

for the H2 and H3 models simulated with quadrilateral elements. These values correspond exactly to the specified specific fracture energy, which verifies the obtained numerical dissipation results for the quadrilateral mesh simulations. The same plausibility check applied to the results obtained with the triangular mesh simulations yields 46 J/m^2 for the H1 model and 43 J/m^2 to 46 J/m^2 for the H2 and H3 models. These slightly higher results could be caused by the curved crack path, which leads to a longer crack line and therefore a higher dissipation result.

5.6. Beam Element Example Problem

At last an example problem for shear flexible Timoshenko beam elements is given in order to demonstrate that the developed damage model can be used for such applications as well. The modeling approach is given in Figure 5.24, where a beam with an applied vertical and horizontal displacement load at the center node of 5 mm and 0.25 mm, respectively, is shown. The horizontal compressive load is required to fully damage the entire cross-section, since the section point located at the neutral axis would not develop damage formation by a bending load alone. The indicated boundary conditions are a horizontally and vertically fixed right node and a left node fixed only in vertical direction. The beam's geometrical dimensions are a length of 800 mm and a quadratic cross-section with a lateral length of 10 mm. The beam is modeled by 32 linear in-plane beam elements (B21). The simulation is performed with an artificial viscosity parameter of $\eta = 1 \times 10^{-4}$ s, a simulation step time of $t_{\text{end}} = 1.0$ s, and the nonlinear geometry option. The used material parameters are given in Table 5.6.

When structural elements such as beam elements are used in conjunction with a UMAT subroutine, Abaqus cannot calculate shear stiffness values during the pre-processing. In case of beam elements, the user must provide the transverse shear stiffness according to the calculation method documented in the Abaqus manual [7]. For the presented problem, a transverse shear stiffness of 276 422 N is used.

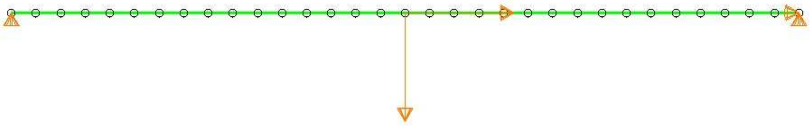

Figure 5.24.: Simulation model for the beam element example problem.

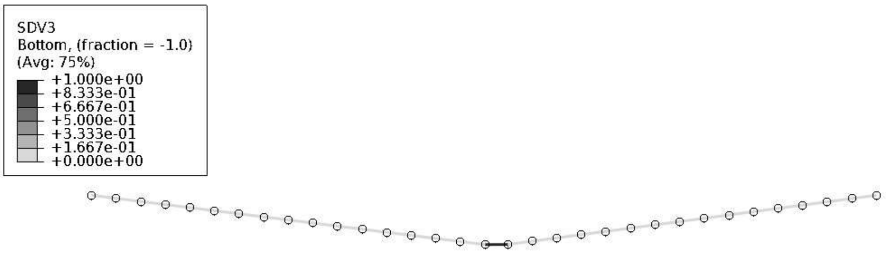

Figure 5.25.: Deformed shape (scaling factor 10x) and viscous damage variable SDV3 distribution for the beam element example problem at the end of the simulation step.

Table 5.6.: Material parameters for the beam elements example problem.

E	ν	ε_0	G_f
20 GPa	0.2	1e-04	$90\,\mathrm{J/m^2}$

Figure 5.25 shows the deformed beam and distribution of the viscous damage variable SDV3. As can be seen, only the element to the right of the center node is damaged. The load-displacement responses in horizontal and vertical direction are given in Figures 5.26 and 5.27, respectively. In addition, the elastic strain energy ALLSE and dissipated energy due to damage formation ALLPD is shown in both figures as well.

The initial linear response to the compressive load can be seen in the horizontal reaction force-displacement diagram, shown in Figure 5.26, which gets followed by a curvature and finally a strain-softening decline once damage formation sets in. The vertical reaction force corresponding to the applied bending deformation, shown in Figure 5.27, exhibits a more complicated curve progression. As can be seen, the applied bending leads to a resisting force in the beginning, which then goes through a transition towards negative values. This means that the beam must be supported to prevent larger bending than the specified displacement load. A common feature of both load-displacement diagrams is the declining reaction force upon damage growth, until finally the reaction force becomes zero. This corresponds to a fully damaged beam element, which can be seen in Figure 5.25.

To verify the obtained results for the energy dissipation due to damage ALLPD, the value at final rupture gets divided by the beam's cross-section

$$\approx \frac{9.1\,\mathrm{mJ}}{100\,\mathrm{mm}^2} = 0.091\,\mathrm{mJ/mm^2} = 91\,\mathrm{J/m^2} \tag{5.7}$$

which is in good agreement to the specified specific fracture energy parameter.

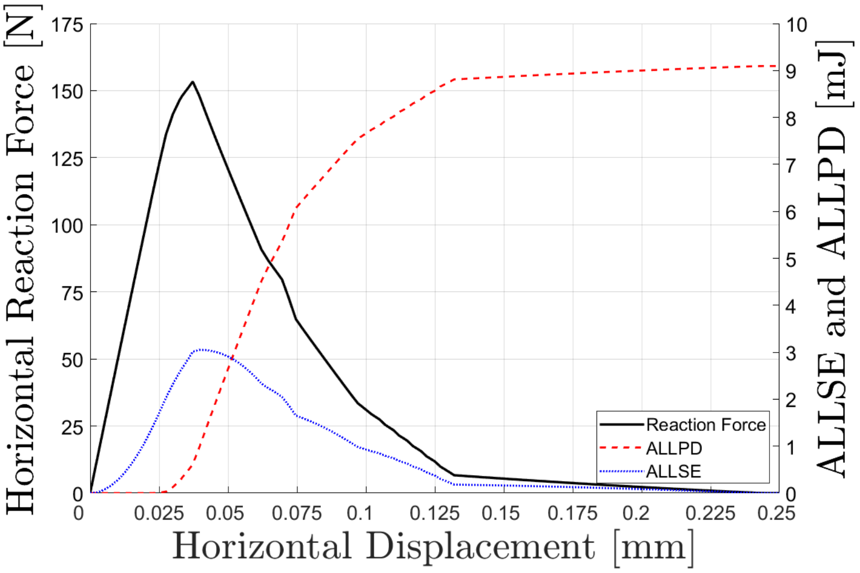

Figure 5.26.: Numerical results showing a load-displacement diagram in horizontal direction.

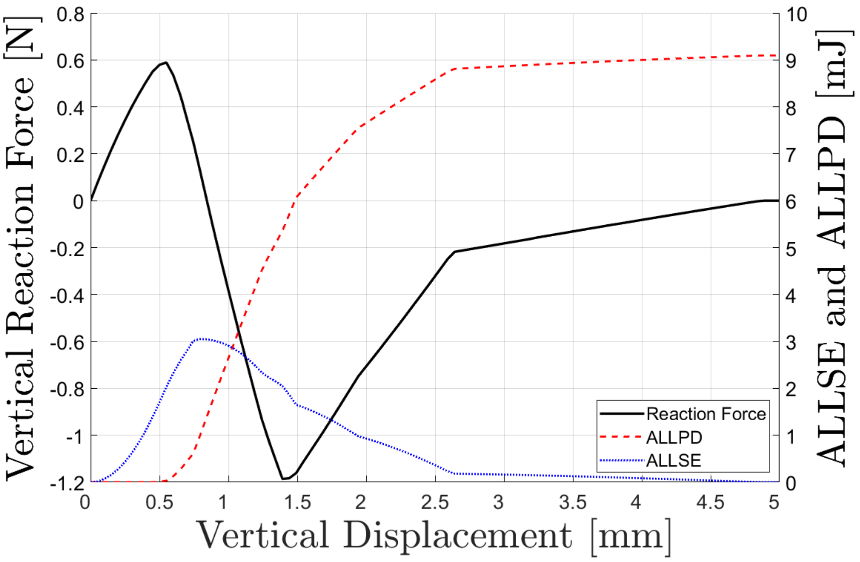

Figure 5.27.: Numerical results showing a load-displacement diagram in vertical direction (force values are shown as positive in displacement direction).

6. Summary and Conclusion

Material damage and the development of crack-like defects are of vital interest for mechanical engineers. Very often these problems are analyzed with numerical methods. To this end, an elasto-damage constitutive law for implicit FEM is developed, implemented, and applied to text book examples within the scope of this thesis. The developed isotropic damage model is based on a continuum damage mechanics description using a single scalar damage variable and a linear strain-softening post-peak response. General strain states are treated by calculating a scalar measure for the strain tensor called equivalent strain, which is calculated with the energy norm. The model is intended for the simulation of damage development in brittle and quasi-brittle materials. Implementation in Abaqus/Standard 2018 by Dassault Systèmes (Vèlizy-Villacoublay, France), a commercial implicit FEM software package, is done via the user material subroutine UMAT. Viscous regularization, which adds an artificial viscosity behavior, ensures that converging results are obtained. Mesh-size dependency typically encountered in FEM simulations of strain-softening materials is alleviated with mesh-adjusted softening regularization. This method incorporates the specific fracture energy and the characteristic element length into the constitutive behavior, where the post-peak softening slope is adjusted in such a manner that mesh-size independent energy dissipation and objective load-displacement results are obtained.

Verification of the developed damage model is done by simulating a uniaxial tensile test of a bar with quadratic cross-section modeled with three different meshes. This simple test proofs that the results are independent of the mesh-size and that the amount of dissipated energy is consistent as it corresponds to the specified specific fracture energy. Additionally, results for two three-point bending tests and a tensile test of a plate with circular hole are compared to literature references made of concrete. The obtained numerical results are in good agreement with the references, which shows that the model yields reasonable results in practical applications. Despite the basic similarities, however, the results also exhibit certain differences compared to the literature references. For example the peak load obtained in both three-point bending tests is lower than in the reference case and the shape of the post-peak region slightly deviates from the reference curve. These differences are attributed to a differently modeled softening regime and a different equivalent strain definition. While the strain-softening behavior is linear in the implemented model, it is exponential in the literature references. Nevertheless, the damage model represents a general elasto-damage constitutive law for isotropic damage, thus the chosen linear strain-softening type is justified.

In conclusion it can be said that the developed constitutive law can be used to simulate damage development until final rupture for brittle and quasi-brittle materials, but it is necessary to keep in mind its limitations. For example mesh-size sensitivity is only avoided if the requirement imposed by the mesh-adjusted softening regularization is fulfilled. Namely that the width of failed elements must be used as length parameter in the regularization procedure, which is only the case when damage localizes into a single layer of quadrilateral or hexahedral elements with an aspect ratio of one. If other elements are used, or if the crack propagates diagonally through the mesh, then it is required to use a correction factor for the length parameter used in the mesh-adjusted softening regularization. This correction factor accounts for the deviation between the characteristic element length and the actual width of damage localization.

Bibliography

[1] A. Hillerborg et al. Analysis of crack formation and crack growth in concrete by means of fracture mechanics and finite elements. *Cement and Concrete Research*, 6:773–782, 1976.

[2] A.A. Griffith. The phenomena of rupture and flow. *Philosophical Transactions of the Royal Society of London. Series A, Containing Papers of a Mathematical or Physical Character*, 221:163–198, 1921.

[3] C. Comi. Part I: Continuum damage models for quasi-brittle materials. In *Damage Models For Concrete Like Materials*, 19th CISM-ITAM Summer School on Variational Approaches To Damage In Continua And Interfaces, Udine, June 2013.

[4] C. Comi. Part II: Strain localization and regularization methods. In *Damage Models For Concrete Like Materials*, 19th CISM-ITAM Summer School on Variational Approaches To Damage In Continua And Interfaces, Udine, June 2013.

[5] C.G. Hoover, Z.P. Bažant. Cohesive crack, size effect, crack band and work-of-fracture models compared to comprehensive concrete fracture tests. *International Journal of Fracture*, 187:133–143, 2014.

[6] C.T. Sun, Z.-H. Jin. *Fracture Mechanics*. Academic Press, 2011.

[7] Dassault Systèmes. Abaqus 6.14 online documentation, 2014. http://ivt-abaqusdoc.ivt.ntnu.no:2080/v6.14/index.html.

[8] D.J. Burnett, H.L. Schreyer. A mesh objective method for modeling crack propagation using the smeared crack approach. *International Journal for Numerical Methods in Engineering*, 117(5):574–603, 2019.

[9] D.S. Dugdale. Yielding of steel sheets containing slits. *Journal of the Mechanics and Physics of Solids*, 8:100–104, 1960.

[10] E.J. Pineda, B.A. Bednarcyk, A.M. Waas, S.M. Arnold. Implementation of a smeared crack band model in a micromechanics framework. Technical Report NASA/TM—2012-217603, NASA, 2012.

[11] G. Pijaudier-Cabot, Z.P. Bazant, M. Tabbara. Comparison of various models for strain-softening. *Engineering Computations*, 5(2):141–150, 1988.

[12] G.I. Barenblatt. The mathematical theory of equilibrium cracks in brittle fracture. *Advances in Applied Mechanics*, 7:55–129, 1962.

[13] G.R. Irwin. Analysis of stresses and strains near the end of a crack traversing a plate. *Journal of Applied Mechanics*, 24:361–364, 1957.

[14] H. Pettermann. Advanced material models for structural analysis, 2019. TU Wien, Lecture Notes, LVA 317.536.

[15] H. Yu, J.S. Olsen, V. Olden, A. Alvaro, J. He, Z. Zhang. Viscous regularization for cohesive zone modeling under constant displacement: An application to hydrogen embrittlement simulation. *Engineering Fracture Mechanics*, 166:23–42, 2016.

[16] J.G. Rots, J. Blaauwendraad. Crack models for concrete: Discrete or smeared? fixed, multi-directional or rotating? *Heron*, 34(1), 1989.

[17] D. Krajcinovic. Damage mechanics. *Mechanics of Materials*, 8:117–197, 1989.

[18] J. Lemaitre. *A Course on Damage Mechanics*. Springer Berlin Heidelberg, 1996.

[19] L.M. Kachanov. Rupture time under creep conditions. *Izvestiia Akademii Nauk SSSR, Otdelenie Teckhnicheskikh Nauk*, 8:26–31, 1958.

[20] M. Jirasek. *Modeling of Localized Inelastic Deformation.* Czech Technical University in Prague, Lecture Notes, 2017.

[21] M. Kurumatani, K. Terada, J. Kato, T. Kyoya, K. Kashiyama. An isotropic damage model based on fracture mechanics for concrete. *Engineering Fracture Mechanics*, 155:49–66, 2016.

[22] M. Todt. Nonlinear finite element method. TU Wien, Lecture Notes, LVA 317.535, 2018.

[23] Sumio Murakami. *Continuum Damage Mechanics - A Continuum Mechanics Approach to the Analysis of Damage and Fracture.* Springer, 2012.

[24] R. de Borst. Some recent developments in computational modelling of concrete fracture. *International Journal of Fracture*, 86:5–36, 1997.

[25] R. de Borst. Fracture in quasi-brittle materials: a review of continuum-damage based approaches. *Engineering Fracture Mechanics*, 69:95–112, 2002.

[26] R. de Borst, J.J.C. Remmers, A. Needleman. Mesh-independent discrete numerical representations of cohesive-zone models. *Engineering Fracture Mechanics*, 73:160–177, 2006.

[27] R. de Borst, J.J.C. Remmers, A. Needleman, M.-A. Abellan. Discrete vs smeared crack models for concrete fracture: bridging the gap. *International Journal for Numerical and Analytical Methods in Geomechanics*, 28:583–607, 2004.

[28] R. de Borst, M.A. Crisfield, J.J.C. Remmers, C.V. Verhoosel. *Non-Linear Finite Element Analysis Of Solids And Structures.* John Wiley & Sons Ltd, 2012.

[29] R. Vignjevic, N. Djordjevica, T. De Vuysta, S. Gemkowb. Modelling of strain softening materials based on equivalent damage force. *Heron*, 335:52–68, 2018.

[30] F.G. Rammerstorfer. Einführung in die finite elemente methoden. TU Wien, Vorlesungsbehelf zur Vorlesung, LVA 317.016, 2014.

[31] R.J. Bulbes. *Troubleshooting Finite-Element Modeling with Abaqus.* Springer Nature Switzerland AG 2020, 2020.

[32] S. Fichant, C. La Borderie, G. Pijaudier-Cabot. Isotropic and anisotropic descriptions of damage in concrete structures. *Mechanics of cohesive-frictional Materials*, 4:339–359, 1999.

[33] T. Belytschko et al. A finite element method for crack growth without remeshing. *International Journal for Numerical Methods in Engineering*, 46:131–150, 1999.

[34] U. Häussler-Combe. *Computational Methods for Reinforced Concrete Structures.* Wilhelm Ernst & Sohn, Verlag für Architektur und technische Wissenschaften GmbH & Co. KG, 2015.

[35] Y.N. Rabotnov. *Creep problems in structural members.* North-Holland Series in Applied Mathematics and Mechanics, 1969.

[36] Z.P. Bazant. Mechanics of distributed cracking. *Applied Mechanics Review*, 39:1–30, 1986.

[37] Z.P. Bazant, B.H. Oh. Crack band theory for fracture of concrete. *Materials and Structures*, 16:155–177, 1983.

[38] Z.P. Bazant, G. Pijaudier-Cabot. Measurement of characteristic length of nonlocal continuum. *Journal of Engineering Mechanics*, 115(4), 1989.

A. Appendix

A.1. Stiffness Tensor $\underset{\approx}{\mathbb{E}}$ and Matrix $\underline{\underline{\boldsymbol{E}}}$

The stiffness tensor that is used in the mechanical constitutive equations is a tensor of fourth-order, which means it has $3^4 = 81$ entries

$$\underset{\approx}{\mathbb{E}}^0 = \begin{bmatrix} E_{1111} & E_{1122} & E_{1133} & E_{1112} & E_{1121} & E_{1123} & E_{1132} & E_{1131} & E_{1113} \\ E_{2211} & E_{2222} & E_{2233} & E_{2212} & E_{2221} & E_{2223} & E_{2232} & E_{2231} & E_{2213} \\ E_{3311} & E_{3322} & E_{3333} & E_{3312} & E_{3321} & E_{3323} & E_{3332} & E_{3331} & E_{3313} \\ E_{1211} & E_{1222} & E_{1233} & E_{1212} & E_{1221} & E_{1223} & E_{1232} & E_{1231} & E_{1213} \\ E_{2111} & E_{2122} & E_{2133} & E_{2112} & E_{2121} & E_{2123} & E_{2132} & E_{2131} & E_{2113} \\ E_{2311} & E_{2322} & E_{2333} & E_{2312} & E_{2321} & E_{2323} & E_{2332} & E_{2331} & E_{2313} \\ E_{3211} & E_{3222} & E_{3233} & E_{3212} & E_{3221} & E_{3223} & E_{3232} & E_{3231} & E_{3213} \\ E_{3111} & E_{3122} & E_{3133} & E_{3112} & E_{3121} & E_{3123} & E_{3132} & E_{3131} & E_{3113} \\ E_{1311} & E_{1322} & E_{1333} & E_{1312} & E_{1321} & E_{1323} & E_{1332} & E_{1331} & E_{1313} \end{bmatrix} \tag{A.1}$$

which are linked by certain symmetry properties. First of all $\underset{\approx}{\mathbb{E}}^0$ possesses minor symmetry $E_{ijkl} = E_{jikl} = E_{ijlk}$, which can be derived from the linear-elastic constitutive equations in index-notation $\sigma_{ij} = E_{ijkl}\varepsilon_{kl}$ and the stress and strain tensor symmetry ($\sigma_{ij} = \sigma_{ji}$, $\varepsilon_{ij} = \varepsilon_{ji}$). And secondly it possesses major symmetry $E_{ijkl} = E_{klij}$.

If these symmetry properties are used and the shear strain components are replaced with the shear angles $\gamma_{ij} = \varepsilon_{ij} + \varepsilon_{ji}$, then the constitutive equation can be written in the form

$$\begin{aligned}\sigma_{ij} = E_{ijkl}\varepsilon_{kl} =& E_{ij11}\varepsilon_{11} + E_{ij22}\varepsilon_{22} + E_{ij33}\varepsilon_{33} \\ &+ E_{ij12}\gamma_{12} + E_{ij13}\gamma_{13} + E_{ij23}\gamma_{23}\end{aligned} \tag{A.2}$$

which represents a shortened form of the same equation. Writing it in matrix-form we obtain

$$\begin{bmatrix}\sigma_{11}\\ \sigma_{22}\\ \sigma_{33}\\ \sigma_{12}\\ \sigma_{13}\\ \sigma_{23}\end{bmatrix} = \begin{bmatrix} E_{1111} & E_{1122} & E_{1133} & E_{1112} & E_{1113} & E_{1123}\\ E_{2211} & E_{2222} & E_{2233} & E_{2212} & E_{2213} & E_{2223}\\ E_{3311} & E_{3322} & E_{3333} & E_{3312} & E_{3313} & E_{3323}\\ E_{1211} & E_{1222} & E_{1233} & E_{1212} & E_{1213} & E_{1223}\\ E_{1311} & E_{1322} & E_{1333} & E_{1312} & E_{1313} & E_{1323}\\ E_{2311} & E_{2322} & E_{2333} & E_{2312} & E_{2313} & E_{2323}\end{bmatrix} \begin{bmatrix}\varepsilon_{11}\\ \varepsilon_{22}\\ \varepsilon_{33}\\ \gamma_{12}\\ \gamma_{13}\\ \gamma_{23}\end{bmatrix} \tag{A.3}$$

with

$$\underline{\underline{\boldsymbol{E}}} = \begin{bmatrix} E_{1111} & E_{1122} & E_{1133} & E_{1112} & E_{1113} & E_{1123}\\ E_{2211} & E_{2222} & E_{2233} & E_{2212} & E_{2213} & E_{2223}\\ E_{3311} & E_{3322} & E_{3333} & E_{3312} & E_{3313} & E_{3323}\\ E_{1211} & E_{1222} & E_{1233} & E_{1212} & E_{1213} & E_{1223}\\ E_{1311} & E_{1322} & E_{1333} & E_{1312} & E_{1313} & E_{1323}\\ E_{2311} & E_{2322} & E_{2333} & E_{2312} & E_{2313} & E_{2323}\end{bmatrix} \tag{A.4}$$

as the stiffness matrix. The component ordering corresponds to the convention used in Abaqus [7] and is similar to Voigt notation except that the fourth and sixth component are switched.

A.2. Elasto-Damage Model Input/Output Tables

The developed UMAT subroutine requires the specification of eight material parameters, which are available in the PROPS(NPROPS) array in the subroutine. The first four parameters are indeed material properties, whereas the remaining four parameters are merely a result of the implementation approach. Naturally, the material properties must be defined with a consistent unit scheme. The artificial viscosity parameter should be approximately three orders of magnitude smaller than the simulation step time, otherwise the introduced error is no longer negligible.

Table A.1.: Input parameters required for the application of the developed elasto-damage UMAT subroutine, which are stored in the material property array PROPS(NPROPS).

Nr.	Input Parameter	Explanation
1	E	Young's Modulus
2	ν	Poisson ratio
3	ε_0	strain at ultimate strength (in a uniaxial tensile test)
4	ε_f or G_f	strain at final rupture (in a uniaxial tensile test) or the specific fracture energy, depending on Flag01
5	η	artificial viscosity
6	Flag01	Flag for the activation/deactivation of the mesh-adjusted softening regularization (MASR) (0: MASR not used → ε_f must be specified in Nr.4) (1: MASR is used → G_f must be specified in Nr.4)
7	Flag02	Flag for the activation/deactivation of the Mazars definition for the energy norm of positive strain. See Section 3.3.1. (0: standard energy norm is used) (1: Mazars energy norm of positive strain is used)
8	CF	Correction factor used to compensate a possible deviation between characteristic element length and the element size perpendicular to the developing damage localization zone. See Section 4.2.2.

The available UMAT subroutine specific output of the developed damage model consist of eight parameters, which are saved in the solution-dependent sate variable array STATEV(NSTATV). These output parameters can be separated into those that are required (SDV1, SDV3, SDV6, SDV8) for the functionality of the developed damage model and those that are saved to be available during post-procession (SDV2, SDV4, SDV5, SDV7).

Table A.2.: UMAT subroutine specific output parameters of the developed elasto-damage UMAT subroutine.

Nr.	Output Parameter	Explanation
1	SDV1	historically largest equivalent strain κ
2	SDV2	inviscid damage variable D
3	SDV3	viscous damage variable D_v
4	SDV4	specific dissipation due to damage formation (gets also stored in the SPD variable)
5	SDV5	specific dissipation due to viscous regularization (gets also stored in the SCD variable)
6	SDV6	summed up area under the equivalent stress-strain diagram (specific el. energy + specific dissipation)
7	SDV7	equivalent strain ε_equ
8	SDV8	element status ELSTAT (1: active / 0: deleted)

The global energy output parameters ALLSE, ALLPD, and ALLCD are available during post-processing if they are requested in the Abaqus input file. Abaqus calculates these global values based on the specific variables SSE, SPD, and SDC calculated in the UMAT subroutine. The ALLPD and ALLCD parameters have a different meaning in the implemented damage model than in the general case. Here ALLPD represents the global energy dissipated due to damage formation and ALLCD represents the global energy dissipated due to viscous regularization.

Table A.3.: Global strain energy and global energy dissipation provided by Abaqus based on the specific values calculated during the UMAT subroutine.

Output Parameter	Explanation
ALLSE	global strain energy
ALLPD	global energy dissipated due to damage formation
ALLCD	gloabl energy dissipated due to viscous regularization

A.3. Example Abaqus Input File

In this section an example Abaqus input file for the application of the developed damage model is given. The command that invokes the use of a user material subroutine is **USER MATERIAL*, where the parameter *CONSTANTS* specifies the number of material properties. Furthermore, the commands **DEPVAR* and **INITIAL CONDITIONS* are used to specify the number of solution-dependent state variables and to initialize them.

```
** Input File for one of the Single Element Verification Simulations
** creates a Cube (10x10x10) and applies a uniaxial deformation
*Node, Nset=Nall
1, 0.0, 0.0, 0.0
2, 10.0, 0.0, 0.0
3, 10.0, 10.0, 0.0
4, 0.0, 10.0, 0.0
5, 0.0, 0.0, 10.0
6, 10.0, 0.0, 10.0
7, 10.0, 10.0, 10.0
8, 0.0, 10.0, 10.0
*NSET, Nset=Bottom
1,2,3,4
*NSET, Nset=Left
1,2,5,6
*NSET, Nset=Back
1,4,5,8
*NSET, Nset=Front
2,3,6,7
*Element, Type=C3D8, Elset=Eall
1, 1, 2, 3, 4, 5, 6, 7, 8
*Material, NAME=UserMat
*USER MATERIAL, CONSTANTS=8
** Constants = Number of material parameters
** E, Nu, Eps_0, Eps_f or G_f, eta, Flag01 (0/1 = Eps_f/G_f), Flag02 (0/1 =
```

```
strain/<strain>), correction factor CF
20000.0, 0.2, 1.2e-04, 0.05, 1e-04, 1, 0, 1.0
*DEPVAR
** alternatively: DEPVAR, DELETE=8
** Number of solution dependent variables STATEV(NSTATV)
8
*INITIAL CONDITIONS, TYPE=SOLUTION
**Elset, EPSMAX, D, D_v, SPD, SCD, SSA, EPSEQU, ELSTAT
Eall, 0.0, 0.0, 0.0, 0.0, 0.0, 0.0, 0.0,
1
*SOLID SECTION, Elset=Eall, Material=UserMat
*BOUNDARY
Back, 1, 1
Left, 2, 2
Bottom, 3, 3
*STEP, NAME=STEP-1, NLGEOM=No, INC=500
*STATIC
0.01, 1.0, 1E-05, 0.01
*Boundary
Front, 1, 1, 1.2e-2
*OUTPUT, HISTORY
*ENERGY OUTPUT, ELSET=Eall
ALLSE, ALLPD, ALLCD
*OUTPUT, FIELD
*ELEMENT OUTPUT, ELSET=Eall
S, E, SDV, STATUS
*NODE OUTPUT, NSET=Nall
U, RF, TF
*END STEP
```